https://doi.org/10.5194/egusphere-2026-847
Preprint. Discussion started: 19 February 2026

Valley longitudinal profiles record the fluvial landscape evolution and geological structure of the Gamburtsev Subglacial Mountains, East Antarctica

Guy J. G. Paxman[1], Fiona J. Clubb[1], Stewart S. R. Jamieson[1], Alexander L. Densmore[1]

[1]Department of Geography, Durham University, Durham, DH1 3LE, United Kingdom

Correspondence to: Guy J. G. Paxman (guy.j.paxman@durham.ac.uk)

Abstract. Fluvial valley networks in mountain ranges record the interactions between climate, tectonics, and lithology. While drainage network analysis has transformed our understanding of these interactions in subaerial settings, the landscape evolution of ice-covered orogens is poorly known. The Gamburtsev Subglacial Mountains are a ~600 km-long mountain range situated beneath the East Antarctic Ice Sheet. These mountains were an important nucleation site for the ice sheet approximately 34 million years ago and are now buried beneath ~2 km of ice. Airborne radar surveying has revealed that the Gamburtsevs are characterised by a rugged, incised landscape, but their geological structure and uplift history remain enigmatic. Here we use a compilation of radar survey data to extract and quantify valley longitudinal profiles from the Gamburtsevs and in turn infer details of their tectonic and geomorphic development. We use χ-mapping and stream power incision modelling to show that the morphology of the valley network is largely consistent with fluvial incision that occurred prior to glaciation. In addition, the spatial distribution of channel steepness indices allows us to confirm the position of major geological boundaries at the edges of the mountains. We also use independent estimates of denudation rates to evaluate competing scenarios for the timing of mountain uplift and valley incision, finding that uplift of the modern Gamburtsevs most likely commenced in the Mesozoic. Regional geomorphic analysis suggests that base level for some Gamburtsev fluvial catchments was set by enclosed interior basins associated with extensional faulting. These depocentres may retain detrital sedimentary material eroded from the Gamburtsevs prior to Antarctic glaciation and are potential targets for future sub-ice drilling campaigns.

1 Introduction

The East Antarctic Ice Sheet (EAIS) is the largest ice mass on Earth, with a volume of ~24 million km^3 and a sea-level equivalent of ~52 metres (Pritchard et al., 2025). The EAIS dates back to ca. 34 million years ago (Ma), when a protracted decline in atmospheric CO_2 and global temperatures (Hönisch et al., 2023; Westerhold et al., 2020) reached a threshold that triggered rapid East Antarctic glaciation (DeConto and Pollard, 2003). A positive feedback of increasing ice-surface elevation and mass balance, increasing surface albedo, and decreasing surface temperatures enabled a rapid transition from late Eocene mountain glaciers and ice fields to an early Oligocene continental-scale ice sheet with margins reaching the coast (Coxall et al., 2005; Gulick et al., 2017; Jamieson et al., 2010).

https://doi.org/10.5194/egusphere-2026-847
Preprint. Discussion started: 19 February 2026

The EAIS likely nucleated on regions of high topography, including Dronning Maud Land, the Gamburtsev Subglacial Mountains (GSM), and the Transantarctic Mountains (DeConto and Pollard, 2003; Jamieson et al., 2010), all of which have peaks >3 km above sea level (Pritchard et al., 2025). Uniquely among these regions, the GSM are entirely covered by the EAIS, with no surface outcrop. The GSM are situated beneath Dome A, the highest point on the EAIS (Fig. 1a), and their topography (Fig. 1b) has been partially surveyed using radio-echo sounding (Bell et al., 2011; Ferraccioli et al., 2011), which has revealed a landscape characterised by sharp ridges and steep-sided valleys with up to 1 km of valley-scale relief (Bo et al., 2009; Rose et al., 2013). This landscape is reminiscent of the present-day European Alps and is believed to have been preserved beneath stable, cold-based, non-erosive ice since EAIS growth at ca. 34 Ma (Creyts et al., 2014; Rose et al., 2013).

The GSM are flanked to their north, east, and west by basins of the East Antarctic Rift System (Fig. 1b), a continental rift system that is hypothesised to have formed as a result of Permo-Triassic (ca. 250 Ma) extension and reactivated during Cretaceous (ca. 100 Ma) transtensional deformation (Ferraccioli et al., 2011; Phillips and Läufer, 2009). The rift system exhibits low-magnitude (M_w 2–4) seismicity today (Lough et al., 2018). To the south, the South Pole Basin (SPB) lies sandwiched between the GSM and the Recovery Subglacial Highlands (RSH; Fig. 1b) (Paxman et al., 2019; Young et al., 2025).

Multiple mechanisms have been hypothesised to explain the origin of the GSM, including collisional orogeny, rift-induced uplift, mantle plume activity, and erosionally-driven uplift (An et al., 2015; Ferraccioli et al., 2011; Paxman et al., 2016; Sleep, 2006; Van De Flierdt et al., 2008; Veevers et al., 2008). However, the absence of *in situ* bedrock samples from the GSM means that their geological structure and the evolution of the landscape prior to glaciation are poorly understood, with tectonic interpretations relying largely on gravity and magnetic surveying (Ferraccioli et al., 2011) (cf. Fig. 1c). As a result, fundamental knowledge gaps about the GSM persist, including their lithological composition, the tectonic and surface processes that have shaped their topography, and the timing of relief generation. There is a need to resolve these unknowns as they will have directly influenced the climatic threshold for EAIS nucleation, early ice-flow directions and thickness patterns, and the pace of the transition from mountain glaciation to continental-scale ice coverage (DeConto and Pollard, 2003; Jamieson et al., 2010; Rose et al., 2013), all of which remain poorly understood.

The well-imaged valley network within the Gamburtsevs (Fig. 1b) offers a valuable opportunity to address these questions. Fluvial valley networks are ubiquitous in subaerial mountain ranges and evolve in response to the balance between rock uplift and erosion (Howard, 1994). Analysis of their planform networks and longitudinal profiles has transformed our understanding of the tectonic and topographic evolution of those areas (Lague, 2014; Whipple and Tucker, 1999). In particular, the morphology of river longitudinal profiles, including their steepness and concavity, has been used to quantify spatiotemporal variations in tectonic rock uplift rate, climate and erosion rates, and lithology in a wide range of subaerial settings (Duvall et al., 2004; Goren et al., 2014; Wobus et al., 2006). However, this approach has not been applied to a subglacial mountain range.

https://doi.org/10.5194/egusphere-2026-847
Preprint. Discussion started: 19 February 2026

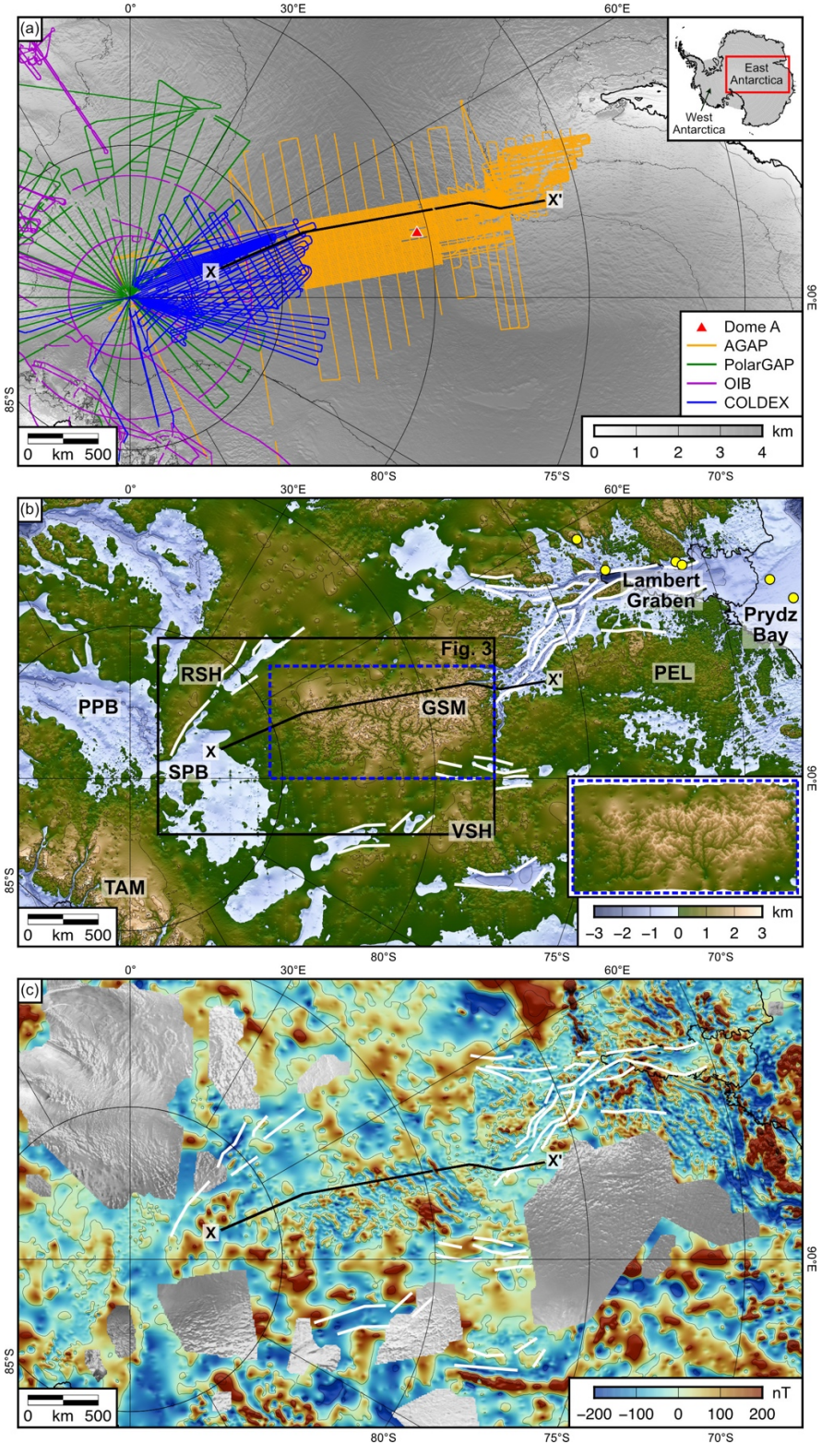

https://doi.org/10.5194/egusphere-2026-847
Preprint. Discussion started: 19 February 2026

Figure 1: Regional setting of the Gamburtsev Subglacial Mountains. (a) Airborne radio-echo sounding surveys used in this study, overlain on hillshaded surface elevation from the Reference Elevation Model of Antarctica (contour interval = 1 km) (Howat et al., 2019). Thick black line marks the grounding line (MEaSUREs version 2). Inset shows the study area within East Antarctica. (b) Bed elevation relative to mean sea level from Bedmap3 (contour interval = 1 km) (Pritchard et al., 2025). Profile X–X' is displayed in Fig. 2; black box shows the extent of Fig. 3. White lines mark the East Antarctic Rift System (Ferraccioli et al., 2011). Yellow circles mark offshore sediment core and onshore moraine locations where samples have been collected for detrital thermochronological analysis (Thomson et al., 2013). Abbreviations: GSM = Gamburtsev Subglacial Mountains; PEL = Princess Elizabeth Land; PPB = Pensacola-Pole Basin; RSH = Recovery Subglacial Highlands; SPB = South Pole Basin; TAM = Transantarctic Mountains; VSH = Vostok Subglacial Highlands. Inset shows a perspective image of the Gamburtsevs (covering the dashed blue area). The topography is viewed from an azimuth of 180° and an angle of 70°, with ~20x vertical exaggeration. (c) ADMAP-2B magnetic anomaly compilation (contour interval = 200 nT) (Eagles et al., 2024; Golynsky et al., 2018). Data gaps are filled by the RADARSAT RAMP AMM-1 SAR image mosaic version 2 (Jezek et al., 2013).

The aim of this study is to understand the tectonic and fluvial controls on the topographic evolution of the Gamburtsevs via analysis of valley longitudinal profiles. The objectives of this analysis are to:

1. Constrain the geological structure of the GSM;
2. Ascertain whether the GSM exhibit a steady-state or transient fluvial landscape morphology and place constraints on their age;
3. Examine the influence of regional tectonics on base level and sediment routing; and
4. Assess the degree to which the landscape was modified by early mountain glaciation.

2 Geophysical Data

2.1 Radio-echo sounding

For this study, we used bed elevation measurements derived from four airborne radio-echo sounding (RES) surveys (Fig. 1a), with details on survey instrumentation provided in the references listed:

- AGAP (Antarctica's Gamburtsev Province) 2007/08 (Bell et al., 2011; Ferraccioli et al., 2011)
- PolarGAP 2015/16 (Paxman et al., 2019; Winter et al., 2018)
- Operation IceBridge 2010, 2014, 2016, 2017, and 2018 (MacGregor et al., 2021)
- COLDEX (Centre for Oldest Ice Exploration) 2022/23 and 2023/24 (Young et al., 2025)

All surveys determined ice thickness along flight tracks by calculating the two-way travel time of radar reflections at the ice surface and bed interfaces. Bed elevation relative to the WGS84 ellipsoid was computed by subtracting the ice thickness from the surface elevation (as measured by the survey). Positional data (latitude, longitude, and height referenced to the WGS84 ellipsoid) were recorded using dual-frequency GPS with an absolute accuracy of <1 m. Although the surveys employed different radar platforms (see the Supplement), the centre frequencies and processing steps were similar, and each survey had an along-track trace spacing (horizontal sampling rate) of 15–30 m and a vertical resolution of ~10 m. Therefore, differences

https://doi.org/10.5194/egusphere-2026-847
Preprint. Discussion started: 19 February 2026

in subglacial topography arising from survey-specific variations in radar instrumentation and processing are likely negligible at the scale of investigation in this study (>100s of metres).

Together, these surveys (Fig. 1a) have excellent coverage of the core massif of the GSM, along with the Lambert Graben to the north, the Gamburtsev foothills to the south, and the SPB and RSH (Fig. 1b; Fig. 2). In these regions of relatively dense RES coverage, flight line spacing is ~5 km. However, coverage to the east and west of the GSM is limited to a small number of widely spaced (~66 km) AGAP reconnaissance lines, making the sub-ice topography difficult to resolve in these areas (Fig. 1a, b). We transformed geographic (latitude and longitude) positional data into x/y co-ordinate pairs in the EPSG:3031 WGS84 / Antarctic Polar Stereographic projection and shifted all ice surface and bed elevation values onto the EIGEN-GL04C geoid (i.e., mean sea level) to ensure consistency with the Bedmap3 continental DEM (Pritchard et al., 2025).

2.2 Magnetic anomalies

To aid interpretations of sub-ice geological structure, we used ADMAP-2B, the most recent compilation of magnetic anomalies for the Antarctic (Eagles et al., 2024; Golynsky et al., 2018). The ADMAP-2B compilation contains near-surface (primarily airborne and shipborne) magnetic anomaly data south of 60°S gridded at an interval of 1.5 km and low-pass filtered for wavelengths >7 km (Fig. 1c). Some gaps in the vicinity of the South Pole have been partially filled by data acquired since the publication of ADMAP-2B (Frémand et al., 2022). However, the ADMAP-2B coverage over the Gamburtsev region is sufficient for the purposes of this study. We used the ADMAP-2B data to identify changes in the intensity and structural pattern of the magnetic anomalies (e.g., Fig. 2) that may reflect the presence of major geological boundaries beneath the ice sheet.

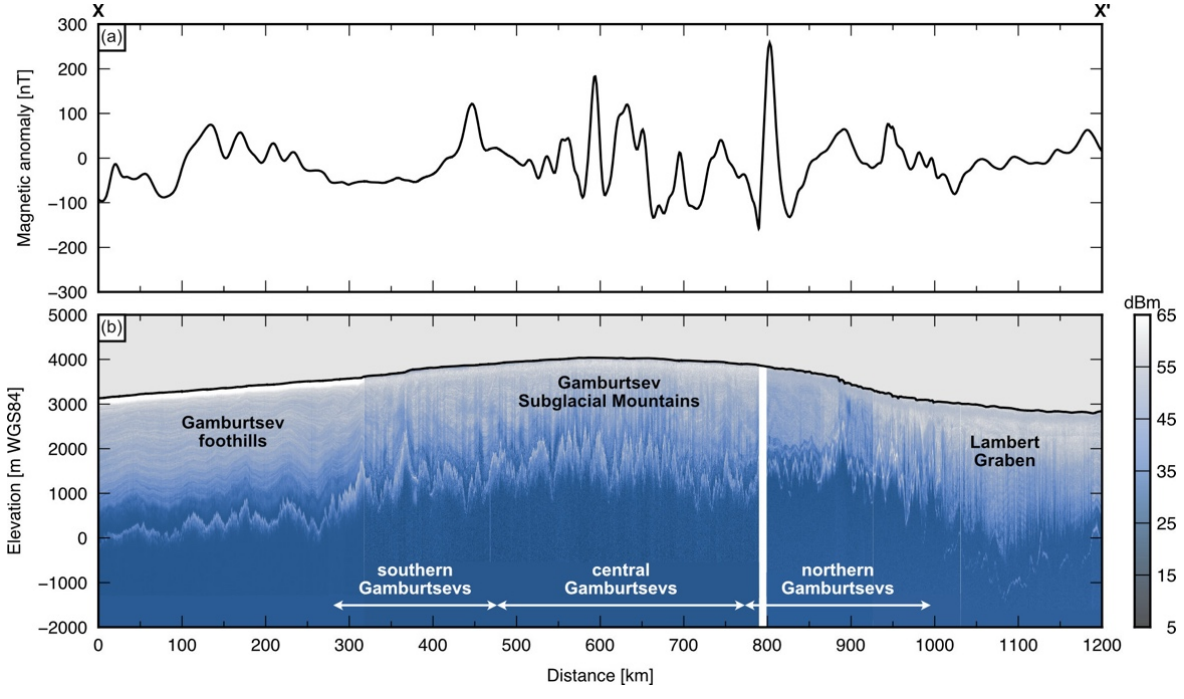

https://doi.org/10.5194/egusphere-2026-847
Preprint. Discussion started: 19 February 2026

Figure 2: Cross-section of the Gamburtsev Subglacial Mountains. Location of profile X–X' is shown in Fig. 1. (a) Magnetic anomaly sampled from the ADMAP-2B compilation (Eagles et al., 2024; Golynsky et al., 2018). (b) Depth-corrected radargram across the Gamburtsevs with ~50x vertical exaggeration. Black line marks the ice surface; elevations are relative to the WGS84 ellipsoid. Colour scale represents the power of the radar return (in decibel-milliwatts); vertical white line at ~800 profile-km is a data gap.

3 Methods

3.1 Valley longitudinal profile extraction

The approximate locations of the valleys within the Gamburtsevs can be identified by visual inspection of the Bedmap3 DEM (Fig. 1b), which we used to guide a systematic search of RES lines. We extracted the (x, y) co-ordinates and bed elevation (relative to the EIGEN-GL04C geoid) of the lowest measured bed elevation from the RES profiles that intersect each valley as a measure of valley floor position and elevation. Since we were primarily interested in valley incision prior to ice-sheet growth, bed elevations were isostatically adjusted to account for the unloading of the Antarctic Ice Sheet. To do so, we used a model for the isostatic response to complete deglaciation (Paxman et al., 2022). For the purposes of subsequent hydrological analysis (section 3.2), we also generated a rebounded version of the Bedmap3 DEM (Fig. 3) using the same approach, with a horizontal resolution of 500 m (Pritchard et al., 2025). No adjustment was made for post-34 Ma erosional modification of the valley floors; we examine the potential impact of this process in section 5.1 of the Discussion.

Due to the limited spatial extent of the RES surveys, valley identification was primarily confined to the AGAP grid, except for the well-surveyed area between 84°S and 88°S that contains lines from all four surveys (Fig. 3a). In total, we identified 937 individual valley floor locations (Fig. 3a). The valleys were organised into 10 basins, each characterised by a trunk valley (defined as the longest continuous pathway) and tributaries. We mapped two orders of tributary upstream of the trunk valley; lower-order headwater channels were not mapped as they were not consistently visible at the resolution of the RES data.

We then connected the RES point measurements to generate a two-dimensional planform network (Fig. 3b). This was guided by computing the hydrological drainage network for the rebounded Bedmap3 DEM. The DEM was filled to remove hydrological sinks, and the flow direction was determined assuming water is routed downslope from each pixel to its lowest neighbour (using a D8 algorithm). We then computed the upstream accumulation area for each grid cell and extracted a hydrological network assuming an upstream area threshold for channel initiation of 50 km^2 (200 cells; Fig. S1a in the Supplement), which we found produced a network of similar resolution to that which was mappable using RES data. These calculations were performed using TopoToolbox version 3 (Schwanghart and Scherler, 2014). For each basin, we constructed longitudinal profiles (upstream distance vs. elevation) for the trunk valley and all tributaries. Only elevations derived from RES point measurements were used to construct these profiles (i.e., elevations were not interpolated between RES lines). The planform network was used to calculate along-profile distance and upstream drainage area, and to differentiate between trunk and tributary valleys. Along-profile distance was set to zero at the first (i.e., furthest downslope) RES-derived point on the trunk valley and increased moving upslope along the thalwegs (Fig. 3b).

https://doi.org/10.5194/egusphere-2026-847
Preprint. Discussion started: 19 February 2026

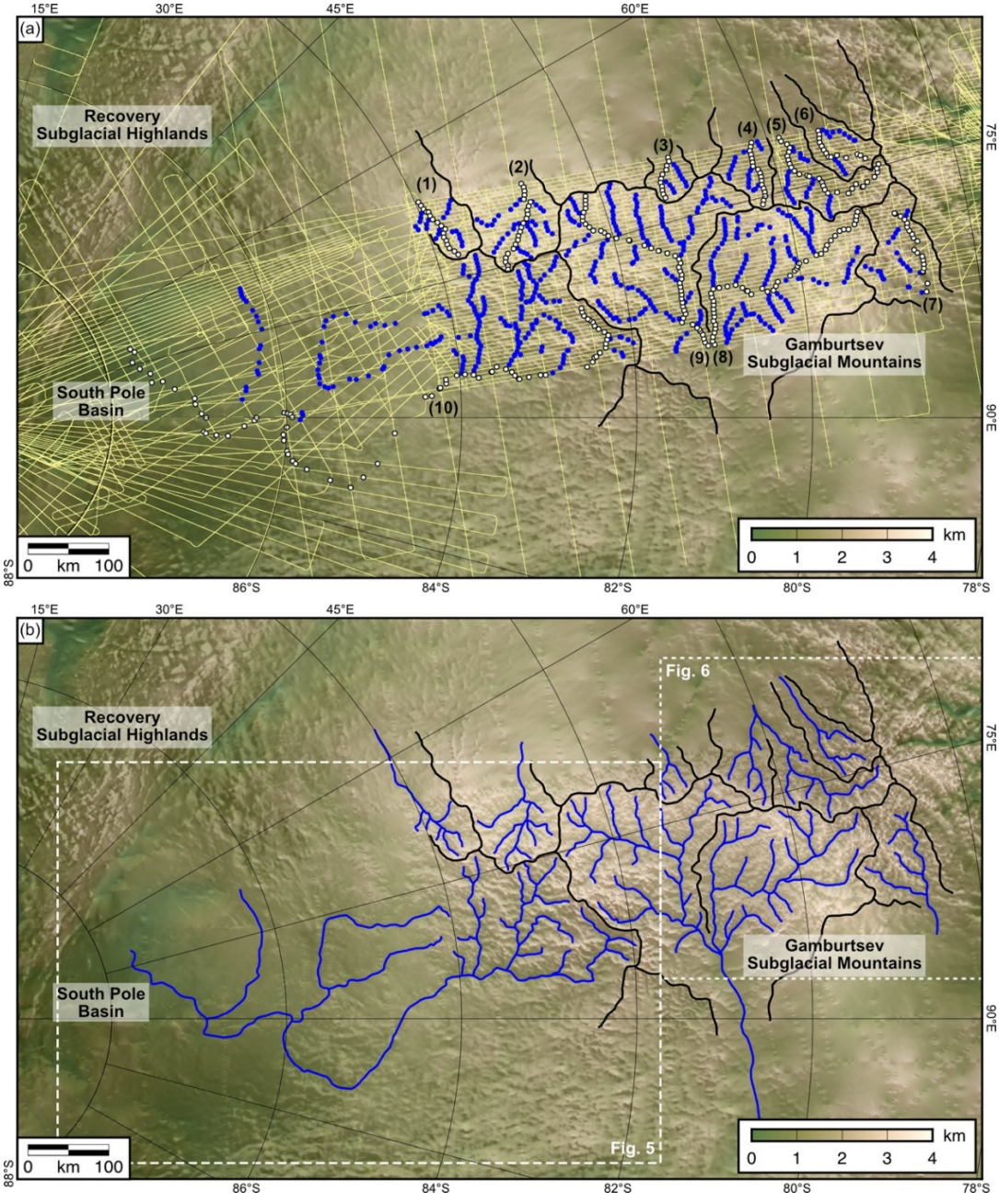

Figure 3: Valley networks in the GSM. (a) Locations of valley floors identified in RES-derived bed elevation data (survey coverage shown in yellow). The mapped valleys are organised into 10 basins (numbered, with black lines marking drainage divides). Circles denote RES measurement points on the trunk (white) and tributary (blue) valleys. (b) Valley planform network (blue lines) derived from RES measurements and hydrological flow routing. For visualisation, some valleys are extrapolated further downslope beyond the lowermost RES point. The underlying bed elevation map is derived from Bedmap3 (Pritchard et al., 2025), isostatically rebounded for ice-sheet removal (Paxman et al., 2022). Shading is from the RADARSAT RAMP AMM-1 SAR image mosaic version 2 (Jezek et al., 2013).

https://doi.org/10.5194/egusphere-2026-847
Preprint. Discussion started: 19 February 2026

3.2 χ analysis

To explore the potential evolution of the GSM, we quantified the shape of valley longitudinal profiles (i.e., the relationship between channel slope and upstream drainage area), allowing us to identify spatiotemporal variations in erosion and/or uplift rate and whether the landscape is likely to be in steady state or shows evidence of transience.

The slope of a river channel (S) at any point is a power law function of the upstream drainage area (A) (Flint, 1974):

$$S = k_s A^{-\theta} \tag{1}$$

where k_s is the channel steepness index and θ is the concavity index.

Expressions for k_s and θ can be derived from the stream power incision model (Howard and Kerby, 1983; Whipple and Tucker, 1999), which assumes that the erosion rate (E) of a river at any point is proportional to the upstream area (A) and slope (S):

$$E = KA^m S^n \tag{2}$$

where m and n are positive exponents and K is an erodibility coefficient that reflects a combination of factors that control erosional efficacy, including bed erodibility, river erosivity, and hydraulic geometry (Lague, 2014). At any point along the profile, the change in elevation (z) with time (t) is given by the difference between the rates of rock uplift (U) and erosion (E):

$$\frac{dz}{dt} = U - E \tag{3}$$

If a river profile is in steady state ($dz/dt = 0$), we can set $U = E$ and rearrange Eq. (2) to form:

$$S = \left(\frac{U}{K}\right)^{1/n} A^{-m/n} \tag{4}$$

From comparison with Eq. (1), we can see that, at steady state:

$$\theta = \frac{m}{n} \tag{5}$$

$$k_s = \left(\frac{U}{K}\right)^{1/n} \tag{6}$$

These two indices define the shape of a river's longitudinal profile (i.e., how channel gradient changes as a function of drainage area). Moreover, since θ is given by the ratio of m and n, and k_s depends on U and K, these indices enable us to extract information pertaining to the tectonic and geological controls on landscape development (Wobus et al., 2006).

To constrain θ and k_s in the GSM, we used the integral approach (χ analysis) (Mudd et al., 2014; Perron and Royden, 2013). We rewrite the slope-area equation as:

$$\frac{dz}{dx} = k_s A^{-m/n} \tag{7}$$

https://doi.org/10.5194/egusphere-2026-847
Preprint. Discussion started: 19 February 2026

and integrate both sides upstream from base level (x_b)

$$\int_{z(x_b)}^{z} dz = \int_{x_b}^{x} k_s A^{-m/n}\, dx \tag{8}$$

which gives

$$z(x) = z(x_b) + \left(\frac{k_s}{A_0^{m/n}}\right)\chi \tag{9}$$

where χ is defined by

$$\chi = \int_{x_b}^{x} \left(\frac{A_0}{A(x)}\right)^{m/n} dx \tag{10}$$

x is the along-profile distance, and A_0 is a reference area introduced to ensure the integrand is dimensionless. We used a standard value of $A_0 = 10^6$ m^2 in all calculations, but the choice is immaterial to the results.

If a fluvial network is in steady state ($U = E$) and the rock uplift rate (U) and erodibility coefficient (K) are uniform in space and time, there should be a single linear relationship between χ and elevation when an appropriate value of θ (m/n) is used. Moreover, tributaries should be collinear with the trunk valley and with each other at the appropriate θ value (Mudd et al., 2014). Since the gradient of the straight line is proportional to k_s (Eq. 9), the χ-elevation plot allows us to independently constrain both θ and k_s. Deviations from a straight line may evidence transient (non-steady-state) evolution of the profile ($U \neq E$) and/or spatial/temporal variations in rock uplift rate or bedrock erodibility (Goren et al., 2014; Perron and Royden, 2013).

We computed χ using the hydrological network determined in section 3.1 and integrating the drainage area in the upstream direction according to Eq. (10) (Fig. S1b) using TopoToolbox version 3 (Schwanghart and Scherler, 2014). We extracted the χ value at each of the 937 RES measurement points on the valley network, and plotted this against rebounded (i.e., ice-free) bed elevation. It is important to note that the drainage network and χ were calculated for a rectangular area of the rebounded Bedmap3 DEM (Fig. S1), such that each basin does not start at the same base level $z(x_b)$, and thus χ values cannot be directly compared between basins. This is because the RES data coverage does not allow us to map most valley networks down to their true base level. However, our analysis focusses solely on the relative changes in χ and channel steepness within each basin, which are independent of the assumed base level.

To determine the best-fitting value of θ for each basin, we calculated χ for θ values between 0 and 1. We then performed a linear least-squares regression of elevation against χ and computed the correlation coefficient (R). The value of θ that best linearises the χ-elevation plot will yield the highest R value. We also computed maximum likelihood estimator and disorder metrics (Hergarten et al., 2016; Mudd et al., 2018) to find the value of θ that best collinearised the trunk valley and tributaries (see the Supplement).

https://doi.org/10.5194/egusphere-2026-847
Preprint. Discussion started: 19 February 2026

For the optimal value of θ, we multiplied the gradient of the χ-elevation regression by $A_0^{m/n}$ to determine k_s (Eq. 9). However, because k_s covaries with θ (Eq. 9), it is not possible to directly compare channel steepness indices from drainage basins with different concavity indices. To isolate the influence of tectonics and lithology on valley profile morphology, it is therefore necessary to compute a normalised channel steepness index (k_{sn}) corresponding to a reference concavity index (θ_{ref}). For this study, we assumed a θ_{ref} of 0.55, which is the mean value across all basins in the Gamburtsevs (median = 0.54; see Table S1 in the Supplement). If there are sections of the channel profile with different k_{sn} values, it is not appropriate to fit a single line through the entire profile (Mudd et al., 2014). Where relevant, we separated the χ-elevation plot into segments where each is characterised by a distinct gradient (i.e., k_{sn}) (Smith et al., 2022).

3.3 Stream power incision modelling

By combining Eq. (2) and (3), we can formulate a partial differential equation that describes the rate of change of river profile elevation through time:

$$\frac{\partial z}{\partial t} = U(t) - KA^m \left(\frac{\partial z}{\partial x}\right)^n \tag{11}$$

This equation is known as the stream power incision model (SPIM) (Whipple and Tucker, 1999) and is widely used to simulate the evolution of fluvial landscapes. We used this equation to forward model longitudinal profiles for the Gamburtsevs in order to: (i) verify whether the shape of the longitudinal profiles is consistent with fluvial incision, and (ii) place limits on the age and uplift history of the landscape using a plausible parameter space constrained as far as possible by observations.

In the SPIM, the constants K, m, and n are interdependent and unique values cannot be retrieved from longitudinal profile modelling alone (Croissant and Braun, 2014). We therefore used the m/n ratio (θ) constrained in section 3.2 and made the common assumption that $n = 1$, meaning $m/n = m$. We assessed the impact of alternative values of n (0.8–1.2) on our results. We then substituted E for U in Eq. (6) and rearranged to form:

$$K = \frac{E}{(k_s)^n} \tag{12}$$

Equation (12) indicates that if we have constrained k_s (for a given m/n), we can back-calculate K if we have an estimate of the average erosion rate (E). Constraining pre-glacial erosion rates for Antarctica, however, is challenging. The only local evidence is derived from detrital thermochronological analysis of Cenozoic clastic sediments in Prydz Bay and nearby coastal moraines (Fig. 1b), which implies long-term catchment-averaged denudation rates of 10–20 m/Myr between the Permo-Triassic (ca. 250 Ma) and the late Eocene (ca. 34 Ma) (Thomson et al., 2013). However, there are reasons to believe that these values underestimate pre-glacial erosion rates for the Gamburtsevs. The recovered erosion rates are at the lower end of the range measured in fluvial drainage basins worldwide (Koppes and Montgomery, 2009). Such low erosion rates are typically confined to catchments with low slopes and relief ratios such as cratonic shields (Portenga and Bierman, 2011; Summerfield and Hulton,

https://doi.org/10.5194/egusphere-2026-847
Preprint. Discussion started: 19 February 2026

1994), which are not consistent with the observed GSM topography. Moreover, the Prydz Bay sediments are situated ~1000 km from the GSM and likely originated from a large source region that includes both the GSM and neighbouring low-relief areas (Jamieson et al., 2005; Taylor et al., 2004). Finally, detrital thermochronology integrates over long time periods; the recovered erosion rates likely therefore reflect a wider regional spatiotemporal average rather than the likely-elevated erosion rates within an active, steep, alpine-style orogen.

Given this uncertainty, we tested two plausible end-member erosion rate scenarios: (i) a low-erosion-rate scenario, with E = 10 m/Myr based on detrital thermochronology (Thomson et al., 2013), and (ii) a high-erosion-rate scenario, with E = 100 m/Myr, which is more consistent with river basins in steep, high-relief, mountainous regions elsewhere on Earth (Koppes and Montgomery, 2009; Summerfield and Hulton, 1994). Global analysis of river basins indicates that the relief ratio (relief / length) of a drainage basin is the strongest predictor of denudation rate (Summerfield and Hulton, 1994). The relief ratio of Gamburtsev basin 10 (the only basin whose extent was fully resolvable) is 0.0028, which corresponds to a denudation rate of ~50 m/Myr using the scaling relationship of Summerfield and Hulton (1994), indicating that our range is suitable. We also note that testing E values spanning one order of magnitude is appropriate given the observed range of denudation rates that can occur for a given basin average slope (Zondervan et al., 2023). For both values of E, we computed the corresponding K using the k_s and θ (with n = 1) recovered from χ analysis. We note that these values of E were used solely for back-calculating K. In our forward models, E is not set and evolves through time in response to U. Determining K in this way also assumes steady-state behaviour over these timescales.

To solve the SPIM, we used a total variation diminishing finite volume method, which is less sensitive to numerical smearing than other partial differential equation solvers and has been demonstrated to produce solutions consistent with analytical methods (Campforts et al., 2017; Campforts and Govers, 2015). The spatial domain of our models was the mapped length of the longitudinal profile. The horizontal resolution was 1 km and the time step was 1 Myr. The initial topography was set to a uniform elevation equal to that of the furthest downslope point on the mapped profile.

We performed two model experiments. First, we assumed that the rock uplift rate (U) was spatially and temporally uniform. We set the total uplift to match the elevation of the highest point on the longitudinal profile and tuned the model run time to best fit the observed profile for the assumed combination of m, n, and K. Second, we performed simulations where pulses of increased rock uplift rate (i.e., base-level fall) were introduced, leading to the generation of propagating knickpoints (see the Supplement). In this situation, the response time (τ_G) for perturbations to propagate upstream from base level (if n = 1) is expressed as (Whipple and Tucker, 1999):

$$\tau_G(x) = \int_0^x \frac{1}{KA(x)^m} dx \tag{13}$$

The response time increases monotonically with x, such that channel reaches farther away from base level have higher response times than lower channel reaches closer to base level.

https://doi.org/10.5194/egusphere-2026-847
Preprint. Discussion started: 19 February 2026

3.4 Regional tectonics and base level

The dense RES survey line coverage between the Gamburtsev foothills and the SPB (Fig. 3) provides an opportunity to assess the regional tectonic structure surrounding the GSM within the wider context of the East Antarctic Rift System (Fig. 1b). We focussed on the potential influence of regional tectonics on: (i) the base level to which valley networks within the GSM may have eroded, and (ii) the location of sediment depocentres within East Antarctica. To do so, we conducted a four-part topographic analysis.

First, we examined the root mean square (RMS) deviation of bed elevation along RES flight tracks over a 400 m length scale (Young et al., 2025), which is a proxy for large-scale roughness of the sub-ice terrain. This may enable identification of (e.g.,) smooth sediment-filled basins. Second, we traced linear features in the RADARSAT RAMP AMM-1 SAR image mosaic (Jezek et al., 2013), which reveals ice-surface undulations that correspond with regions of steep sub-ice topography and may reflect tectonic structures such as faults (Chang et al., 2016). Third, we quantified the along-strike variation in elevation and half-width of the RSH, which can be used to constrain the direction and recency of fault propagation (Densmore et al., 2005, 2007). We sampled elevations from the rebounded Bedmap3 DEM along a swath of 20 profiles oriented parallel to the strike of the range front. RSH half-width was approximated as half the horizontal distance across the region enclosed by the 1500 m contour (under ice-free conditions). Fourth, we used an elastic plate model to compute the flexural response to mechanical unloading (due to extensional faulting) and erosional unloading to evaluate whether these two processes can account for the configuration of the regional topography, as would be expected in a continental rift system setting (Contreras-Reyes and Osses, 2010; Ebinger et al., 1991; Watts, 2023) (see the Supplement).

4 Results

4.1 Longitudinal profile morphology

For each of the 10 drainage basins identified in the GSM (Fig. 3), we extracted the longitudinal profile of the trunk valley and its tributaries (Fig. 4). The number of tributaries mapped per basin ranged between 2 and 18, with a total of 85 distinct valley thalwegs (10 trunks; 75 tributaries) across the 10 basins. The mapped length of the trunk valleys ranged from 54.3 km (basin 3) to 947 km (basin 10). All trunk valley longitudinal profiles exhibit a concave-up morphology, with steeper channel gradients in the upper reaches and lower gradients further down. Tributaries are largely concave-up and smoothly and systematically join the trunk valley in a downslope direction without ‘hanging’ above the trunk (Fig. 4).

https://doi.org/10.5194/egusphere-2026-847
Preprint. Discussion started: 19 February 2026

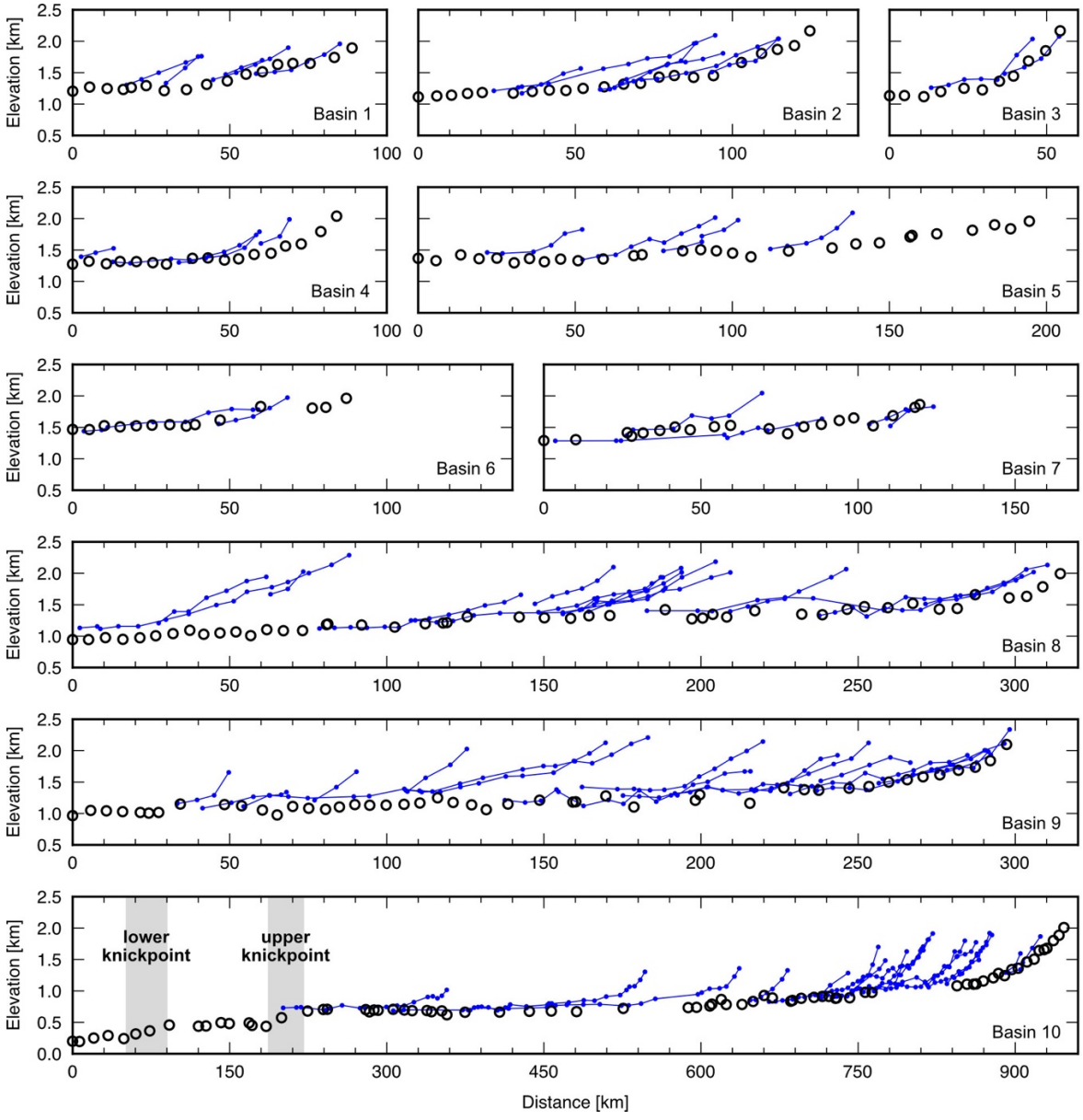

Figure 4: Longitudinal valley profiles for all basins in the GSM. Black circles = trunk valleys; blue circles/lines = tributaries. Elevations are relative to mean sea level and have been isostatically adjusted for the removal of the ice sheet (Paxman et al., 2022). Note that the horizontal scale is the same for each profile except basin 10 (bottom panel). Shaded regions mark the knickpoints mentioned in the text.

We found that the density of RES measurements along the longitudinal profiles was sufficient to capture the morphology of the profiles at length scales appropriate for our analysis. The frequency distribution of the along-thalweg distance between adjacent RES measurements shows a strong modal peak at 5–6 km, reflecting the consistent AGAP grid spacing (Fig. S2). We found that 87% of point spacings are <10 km and 98% are <20 km. Only 8 of the 852 point-spacings exceed 30 km, often occurring in gaps between survey grids or where the valley thalweg runs parallel to survey lines.

https://doi.org/10.5194/egusphere-2026-847
Preprint. Discussion started: 19 February 2026

The highest (furthest upslope) points on the longitudinal profiles are currently situated at elevations of ~1000–1500 m above sea level. However, isostatic adjustment for the removal of the EAIS would contribute ~700 m of uplift across the Gamburtsevs (Paxman et al., 2022). Therefore, under ice-free conditions the upper reaches of the longitudinal profiles would be situated at ~1700–2200 m above sea level (Fig. 4). The longitudinal profiles of basins 1–9 could only be mapped as far downslope as the edges of the AGAP survey grid (Fig. 3a), with a maximum trunk valley thalweg length of 314 km (basin 8). The lowermost mapped valley floors would be situated at ~1000–1500 m above sea level under ice-free conditions (Fig. 4). The upper reaches of the longitudinal profiles in the northern Gamburtsevs (basins 5, 6, 7) appear to be characterised by gentler gradients than those in the central (3, 4, 8, 9) and southern (1, 2, 10) Gamburtsevs (Fig. 4). We also note that not all longitudinal profiles decrease monotonically in elevation moving downslope; several valleys exhibit local minima (i.e., enclosed lows), which often coincide with tributary junctions (e.g., basins 5, 7, and 9), and, less commonly, isolated maxima (e.g., basins 6 and 8).

RES survey coverage allowed us to map the longitudinal profile of basin 10 from the southern Gamburtsevs to the SPB. As well as a well-defined concave-up form, this profile exhibits two ~40 km-long regions of steeper channel gradient, or knickpoints, that separate regions of shallower channel gradient (Fig. 4). The vertical relief (top-to-bottom elevation change) of the 'lower' (situated at ~90 profile-km) and 'upper' (situated at ~220 profile-km) knickpoints are ~260 m and ~210 m, respectively (Fig. 4).

4.2 χ-elevation relationships

Using χ-elevation plots, we were able to constrain θ and k_s for six of the 10 basins (2, 5, 7, 8, 9, and 10), which all yielded θ values that best linearised the χ-elevation plot of between 0.50 and 0.61 (Table S1). The maximum likelihood estimator and disorder metrics also found that the tributaries and the trunk valley were best collinearised in χ-elevation space by similar θ values (Fig. S3). In contrast, the hydrological network and χ calculation in basins 1, 3, 4, and 6 were compromised by these comparatively small catchments being poorly resolved in the Bedmap3 DEM, partially owing to gridding artefacts, meaning that a robust full-basin χ-elevation plot could not be constructed.

For basin 10, we visually identified three linear segments in χ-elevation space: segment 1 is downstream of the upper knickpoint (0–220 profile-km), segment 2 is between 220 and 600 profile-km, and segment 3 is above 600 profile-km (Fig. 5a,b). Segment 3, which contains 185 of the 278 RES measurement points in the basin, returned a best-fitting θ of 0.60 (via the R metric; Fig. 5b). The maximum likelihood estimator and disorder metrics indicated that the trunk valley and tributaries were best collinearised for θ values of 0.58 and 0.57, respectively (Fig. S3), showing that all three methods were in good agreement.

The boundary between segments 2 and 3 is marked by a step-change in k_s, with segment 2 having a value of 782 $m^{1.2}$ and segment 3 a value of 1910 $m^{1.2}$ (for $\theta = 0.60$). The corresponding k_{sn} ($\theta_{ref} = 0.55$) values are 255 $m^{1.1}$ and 667 $m^{1.1}$, respectively.

https://doi.org/10.5194/egusphere-2026-847
Preprint. Discussion started: 19 February 2026

We also found that the upper reaches of two tributaries situated between 520 and 640 profile-km were better fit by a regression line with a gradient equal to that of segment 3 (Fig. 5b, c). Although there is a degree of ambiguity over the exact position of the transition between segments 2 and 3 (Fig. 5b), visual segmentation is sufficient for identifying the approximate location of the boundary (Demoulin et al., 2015; Smith et al., 2022). Moreover, this approach can be validated through comparison with the magnetic anomaly. The boundary between segments 2 and 3 coincides with a marked change in the intensity and structural pattern of the magnetic anomaly. Segment 3 is characterised by short-wavelength (<10 km) anomalies characterised by vertical derivatives of up to ±40 nT/km, whereas the short-wavelength signal is notably muted in segment 2 (Fig. 5c, d, e).

https://doi.org/10.5194/egusphere-2026-847
Preprint. Discussion started: 19 February 2026

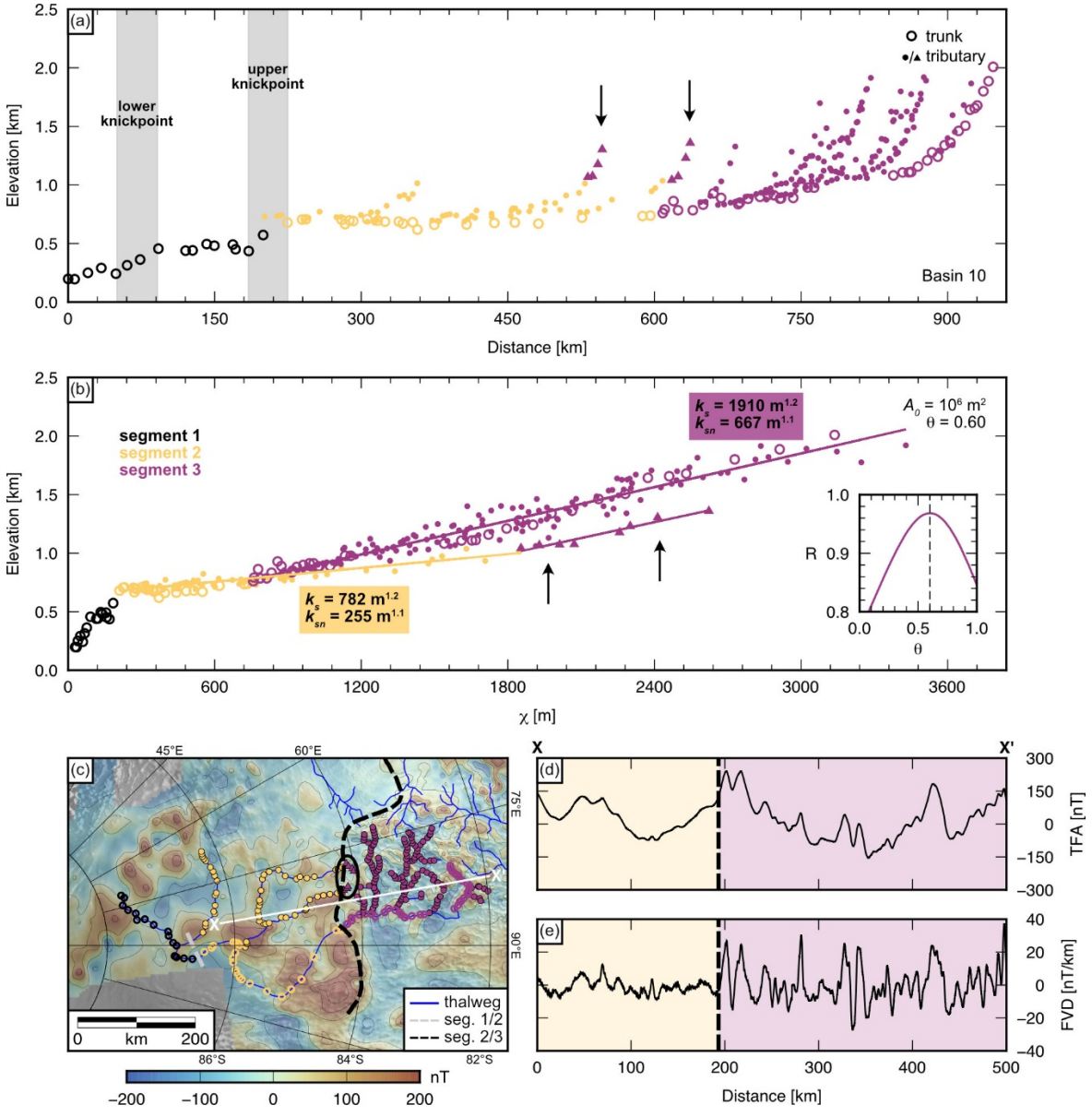

345 **Figure 5: Longitudinal profile analysis in the southern GSM.** (a) Longitudinal distance-elevation profile for basin 10. Colours denote segments of the profile in χ-elevation space. (b) χ-elevation plot, transformed with $A_0 = 10^6$ m^2 and a best-fitting θ (for segment 3) of 0.60. The plot shows three linear segments with distinct gradients. Recovered values for k_s (for $\theta = 0.60$) and k_{sn} (for $\theta_{ref} = 0.55$) are labelled for the two segments above the knickpoints. Note that the upper reaches of two tributaries at approximately 80°E, 84°S (marked by triangle symbols and black arrows) are well fit by a separate regression line with a gradient equal to that of segment 3. Inset: correlation coefficient
350 (R) as a function of θ for linear least-squares regression of segment 3. (c) Valley network overlain on the ADMAP-2B magnetic anomaly (Eagles et al., 2024; Golynsky et al., 2018). Valley floor point colours correspond to those in panels (a) and (b). Heavy dashed lines show boundaries between χ-elevation segments (grey = segments 1 and 2; black = segments 2 and 3). Black oval indicates the location of the tributaries marked in panels (a) and (b). Contour interval is 100 nT. (d) Magnetic anomaly (total field anomaly TFA, in nT) along profile X–X' (location shown in panel c). (e) First vertical derivative (FVD) of the TFA, which enhances the effects of shallow sources. The dashed
355 vertical line marks the boundary between segments 2 and 3 (see panel c).

https://doi.org/10.5194/egusphere-2026-847
Preprint. Discussion started: 19 February 2026

In section 4.1, we noted that longitudinal profiles in the northern GSM appear to have gentler slopes in the upper reaches than those in the central and southern GSM (Fig. 4). However, these slopes cannot be directly compared because the drainage basins have different areas and concavities. χ analysis allows us to normalise for these variables and compare k_{sn} across the northern and central GSM. To do so, we divided the upper reaches of basins 4, 5, 6, 7, and 8 into 22 segments of approximately equal length (~50 km; Fig. 6a) and computed k_{sn} from the χ-elevation plots where $\theta_{ref} = 0.55$ (Fig. S4). We found a dichotomy of k_{sn} values across the northern GSM. Of the 22 segments, 18 were characterised by a k_{sn} of 500–900 $m^{1.1}$, while four were characterised by a value of 300–400 $m^{1.1}$ (Fig. 6b). The four segments with lower steepness indices were clustered in the northernmost GSM. The spatial boundary between the two groups of channel segments coincides with a transition in the intensity and pattern of the magnetic anomaly, with east–west-trending short-wavelength (10–20 km) anomalies with amplitudes of up to ±200 nT to the south and a lower-amplitude signal lacking in lineations to the north (Fig. 6a).

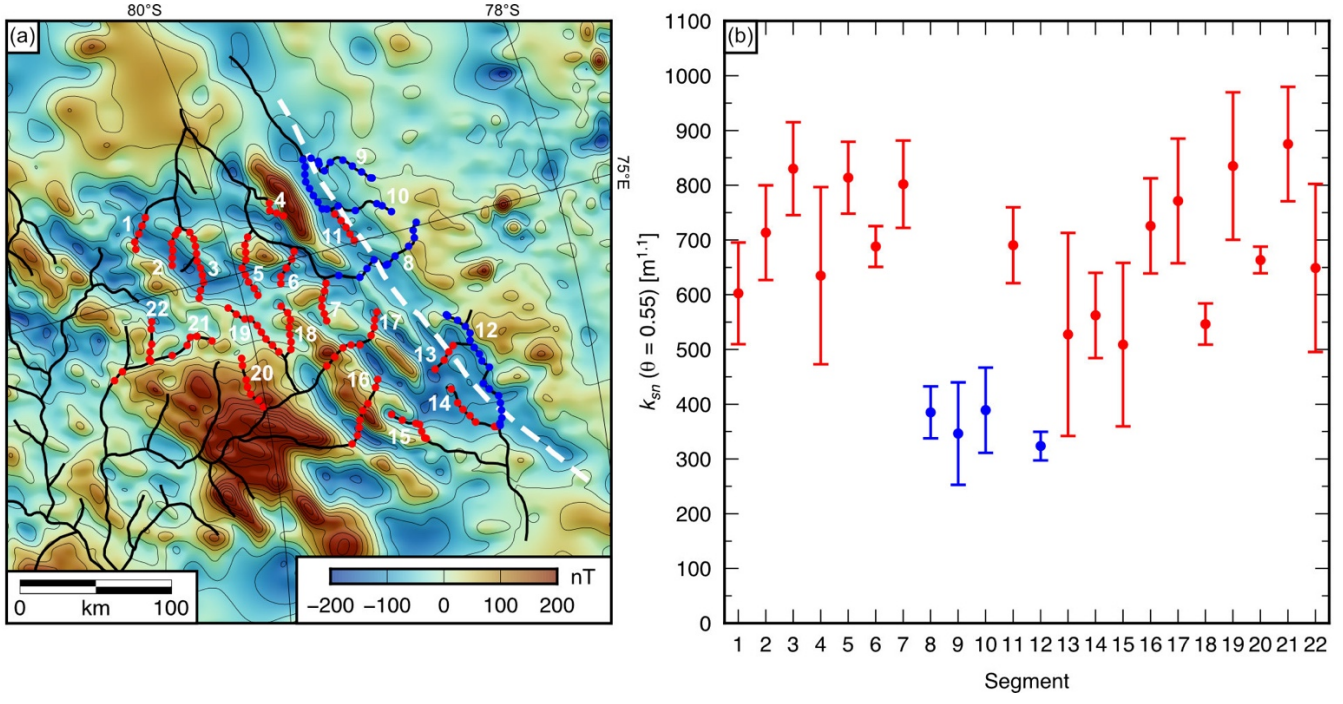

Figure 6: Normalised channel steepness indices in the northern GSM. (a) Valley network (black) with selected segments used for χ analysis (coloured circles and white numbers; see Fig. S4 for χ-elevation plots for individual segments) overlain on the ADMAP-2B magnetic anomaly (Eagles et al., 2024; Golynsky et al., 2018). Contour interval is 50 nT. The dashed white line marks a major magnetic boundary and roughly coincides with the transition from high-k_{sn} valleys to the south (left) to low-k_{sn} values to the north (right). (b) Normalised channel steepness index (k_{sn}; corresponding to $\theta_{ref} = 0.55$) for each of the 22 valley segments. Values of k_{sn} were computed from the gradient of the linear least-squares regression of the χ-elevation plot for each segment. Error bars denote ±1 standard deviation. Blue and red colours denote valley segments differentiated by their k_{sn} values and position relative to the magnetic boundary in panel (a).

https://doi.org/10.5194/egusphere-2026-847
Preprint. Discussion started: 19 February 2026

4.3 Longitudinal profile evolution

Since it was the longest mapped longitudinal profile, we focussed our stream power incision modelling on basin 10. Our first modelling experiment assumed a constant U, m = 0.60, and n = 1 (Eq. 11). However, we note that χ analysis revealed that segments 2 and 3 had different k_s values (Fig. 5b), which (according to Eq. 6) reflects a difference in U and/or K. Given that the boundary between the segments is relatively abrupt, is observed across multiple tributaries within the network, and corresponds with a magnetic anomaly transition (Fig. 5c, d, e), we hypothesise that a lithological boundary with a step-change in K is likely responsible for the different k_s values.

To test this hypothesis, we ran the SPIM for K values corresponding to the k_s values recovered from χ analysis for segments 2 and 3 (Fig. 5b). For these models we calculated K using Eq. (12) for E = 10 or 100 m/Myr (Fig. 7a, b), with K assumed to be spatially uniform over the length of each segment. The computed K values were 1.3 or 13 x 10^{-8} $m^{-0.2}$ / yr for segment 2 and 0.52 or 5.2 x 10^{-8} $m^{-0.2}$ / yr for segment 3. When adjusted for covariance with m, these K estimates are in close agreement with the range derived for granitoids and metasedimentary rocks (Stock and Montgomery, 1999), which have values substantially lower than other lithological groups such as basalts, volcaniclastic rocks, and mudstones (Fig. 7c).

For a given value of E, the modelled longitudinal profile yields a close fit to observed elevations within segments 3 when a lower K value is used, and an improved fit with the more gradual slope of segment 2 when a higher K value is used (Fig. 7a). The range of model run times that yielded the best fit to the observed profile across both segments (by minimising the RMS misfit between the observed and modelled elevations) was 22–216 Myr (Fig. 7d). The model with different K values for segments 2 and 3 has a combined RMS misfit of 36.7 m, which is lower than the misfits if either K value is used for the entire reach. This result confirms the findings of the χ analysis and indicates that the profile likely crosses a lithological boundary with a step-change in K at ~600 profile-km.

However, these simulations cannot account for the presence of the two knickpoints within segment 1, which have higher slopes than the regional trend (Fig. 7a). These features may either: (i) be static due to spatial changes in lithology (K) or rock uplift rate (U), or (ii) reflect a transient response of the profile to base-level fall, having propagated some distance upstream. In our second modelling experiment, we used the SPIM and Eq. (13) to calculate the time taken for the two knickpoints to propagate to their observed positions, assuming they started at base level, which is taken to be the lowermost point on the profile (see section 4.4). For a range of parameter space including E = 10 or 100 m/Myr, m/n = 0.5–0.6, and n = 0.8–1.2, the response times for the lower and upper knickpoints to propagate to their observed locations are 0.18–6.3 Myr and 0.55–18 Myr, respectively (Fig. S5). The variation in E (and therefore K) has the dominant influence on these ranges, with the contributions of m and n to the total range each being ~5x lower. We discuss the origin and significance of the knickpoints in section 5.3.

https://doi.org/10.5194/egusphere-2026-847
Preprint. Discussion started: 19 February 2026

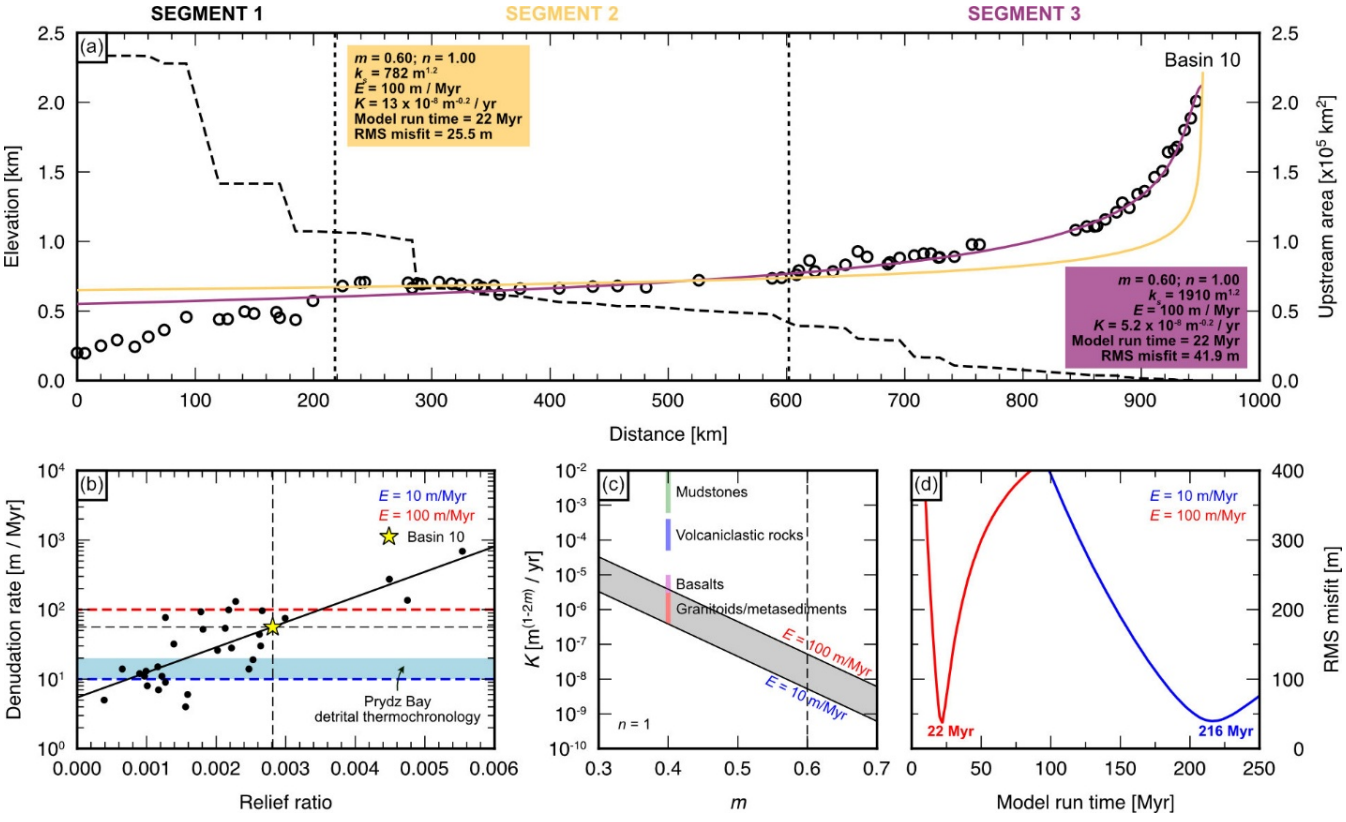

Figure 7: Stream power incision modelling with uniform uplift rate. (a) Comparison between modelled (coloured lines) and observed (circles) longitudinal profiles for basin 10. The stepped dashed line marks the upstream drainage area (right-hand y-axis) as a function of distance along the profile. Vertical dashed lines mark boundaries between profile segments. The models shown used K values calculated assuming E = 100 m/Myr; different values of K are used for segments 2 and 3 depending on k_s. The best-fitting model profiles for E = 10 m/Myr are almost identical but require a ~10x longer model run time (see Fig. S5). (b) Global compilation of river basin denudation rates and relief ratios (Summerfield and Hulton, 1994). Black line was calculated via linear least-squares regression (R = 0.791). Blue horizontal bar denotes long-term catchment-averaged denudation rates (10–20 m/Myr) derived from thermochronological analysis of detrital sediments in Prydz Bay (Thomson et al., 2013). Blue and red dashed lines mark denudation rates of 10 m/Myr and 100 m/Myr, respectively, which were used for the two K scenarios in our models. Yellow star and dashed lines mark a relief ratio of 0.028 (value for basin 10), which corresponds to a denudation rate (E) of ~50 m/Myr. (c) Covariance of K and m. The shaded region corresponds to an E range of 10–100 m/Myr (for the k_s value of segment 3). Coloured horizontal bars denote ranges of K for different lithologies (Stock and Montgomery, 1999) where m = 0.40. Dashed line marks m = 0.60, used in our modelling. (d) RMS misfit between the observed and modelled longitudinal profiles across segments 2 and 3 (panel a) as a function of model run time for the two K scenarios corresponding to E = 10 m/Myr and 100 m/Myr.

https://doi.org/10.5194/egusphere-2026-847
Preprint. Discussion started: 19 February 2026

For catchments in the central GSM (basins 5, 8, and 9), we also generated modelled longitudinal profiles using values of K and m derived from the best-fitting θ and k_s obtained via χ analysis (Fig. 8). These three basins are situated on the southern side of the magnetic anomaly transition identified in Fig. 6a. Basins 5 and 9 were characterised by a single linear segment in χ-elevation space, whereas basin 8 exhibits a second segment in the upper reaches (Fig. 8c). Aside from the upper segment of basin 8, the resulting longitudinal profiles showed good agreement with the observed profiles for best-fitting model run times of up to 167 Myr (Fig. 8). These times are lower than in basin 10, although we note that the trunk valleys of these central catchments are not mapped down to their base level, so shorter timescales are expected. Localised deviations from the modelled profiles are observed, with parts of the observed profiles falling below the models (Fig. 8).

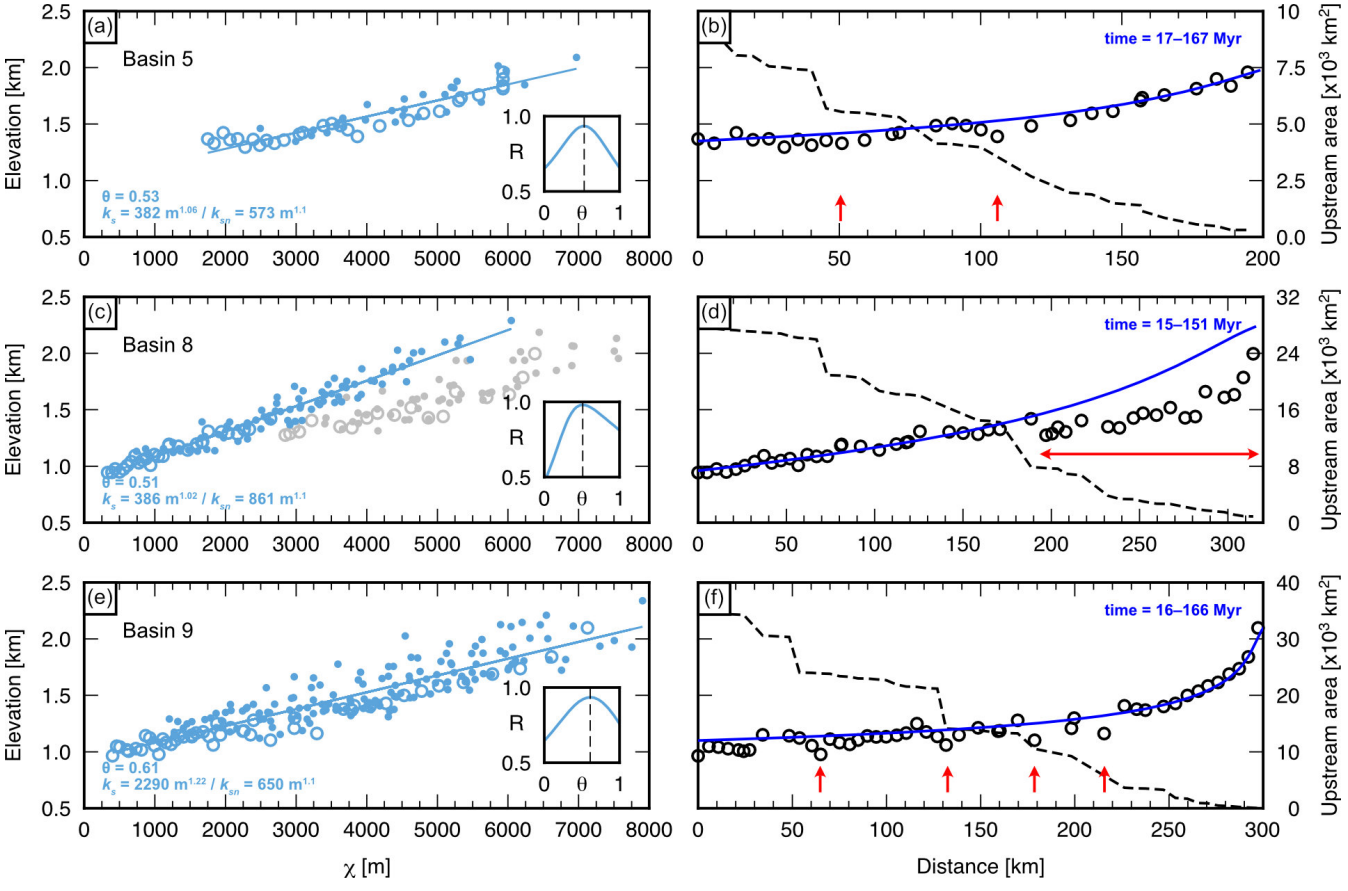

Figure 8: χ analysis and stream power incision modelling in the central GSM. (a) χ-elevation plot for basin 5. Open circles = trunk valley; closed circles = tributaries. Best-fitting θ is identified from the correlation coefficient R (inset plots) of the linear regression (straight line). Recovered k_s and k_{sn} (θ_{ref} = 0.55) are labelled. (b) Modelled longitudinal profile for basin 5 calculated using the recovered θ and k_s (dark blue curve) superimposed on the observed trunk profile (circles). Dashed line denotes upstream drainage area. Red arrows here and in panels (d) and (f) mark deviations from the modelled profile. Model run time is labelled in the upper corner. (c) χ-elevation plot for basin 8. Symbols as for panel a, except grey circles mark points that deviate from the linear part of the plot (blue). (d) Modelled longitudinal profile for basin 8. (e) χ-elevation plot for basin 9. (f) Modelled longitudinal profile for basin 9.

https://doi.org/10.5194/egusphere-2026-847
Preprint. Discussion started: 19 February 2026

4.4 Base level and tectonic structure south of the Gamburtsevs

The region to the south of the Gamburtsevs, where the longitudinal profile of basin 10 appears to terminate, is characterised by a major north–south-trending topographic lineament visible in the RAMP AMM-1 SAR image mosaic (Fig. 9a). To the west of this lineament is the rugged and elevated topography of the RSH, which contrasts with the smoother, low-lying terrain of the SPB east of the lineament (Fig. 9b). The valley network of basin 10 can be traced to a part of the SPB characterised by conspicuously low RMS deviations of bed elevation (<10 m; Fig. 9b), which are indicative of low large-scale (>100 m) roughness (Young et al., 2025). Moreover, RES imaging reveals a bed with high specularity content in this area (>0.4; Fig. S6), which is indicative of low roughness at small (i.e., decimetre) scales (Schroeder et al., 2015; Young et al., 2025). This smooth region, measuring approximately 100 km x 50 km, is contained within an enclosed topographic basin (Fig. S6) and therefore may constitute base level for basin 10.

RES imaging shows that the RSH exhibit an asymmetric cross-sectional profile, with a steep escarpment at their eastern margin that is expressed as the lineament visible in the RAMP AMM-1 SAR image mosaic (Fig. 9a). The highlands are tilted westwards away from the escarpment at an angle of ~0.3° (Fig. 9c, d). Flexural modelling indicates that this topography is consistent with uplift and tilting of the highlands due to a combination of: (i) mechanical unloading on an extensional fault system located at the base of the escarpment and (ii) erosional unloading of material excavated from the large troughs on either side of the highlands (Fig. S7). By computing the theoretical pattern of flexure and comparing to the observed escarpment relief and highland tilt, we recovered a best-fitting effective elastic thickness (*Te*) of 26 km and a faulted layer thickness of 29 km (Fig. 9c, d, e; Fig. S7).

A swath of topographic profiles along-strike of the RSH shows that ice-free elevations increase from ~1000–1200 m at the southern end of the range to ~1500–1700 m to the north (Fig. S8). This change in elevation occurs over a length scale of ~25 km and coincides with an increase in RSH half-width to ~15 km (Fig. S8). The position of this transition in RSH elevation and half-width coincides with the southern edge of the escarpment and the location of the smooth basin on the hanging-wall side of the range front (Fig. S8).

https://doi.org/10.5194/egusphere-2026-847
Preprint. Discussion started: 19 February 2026

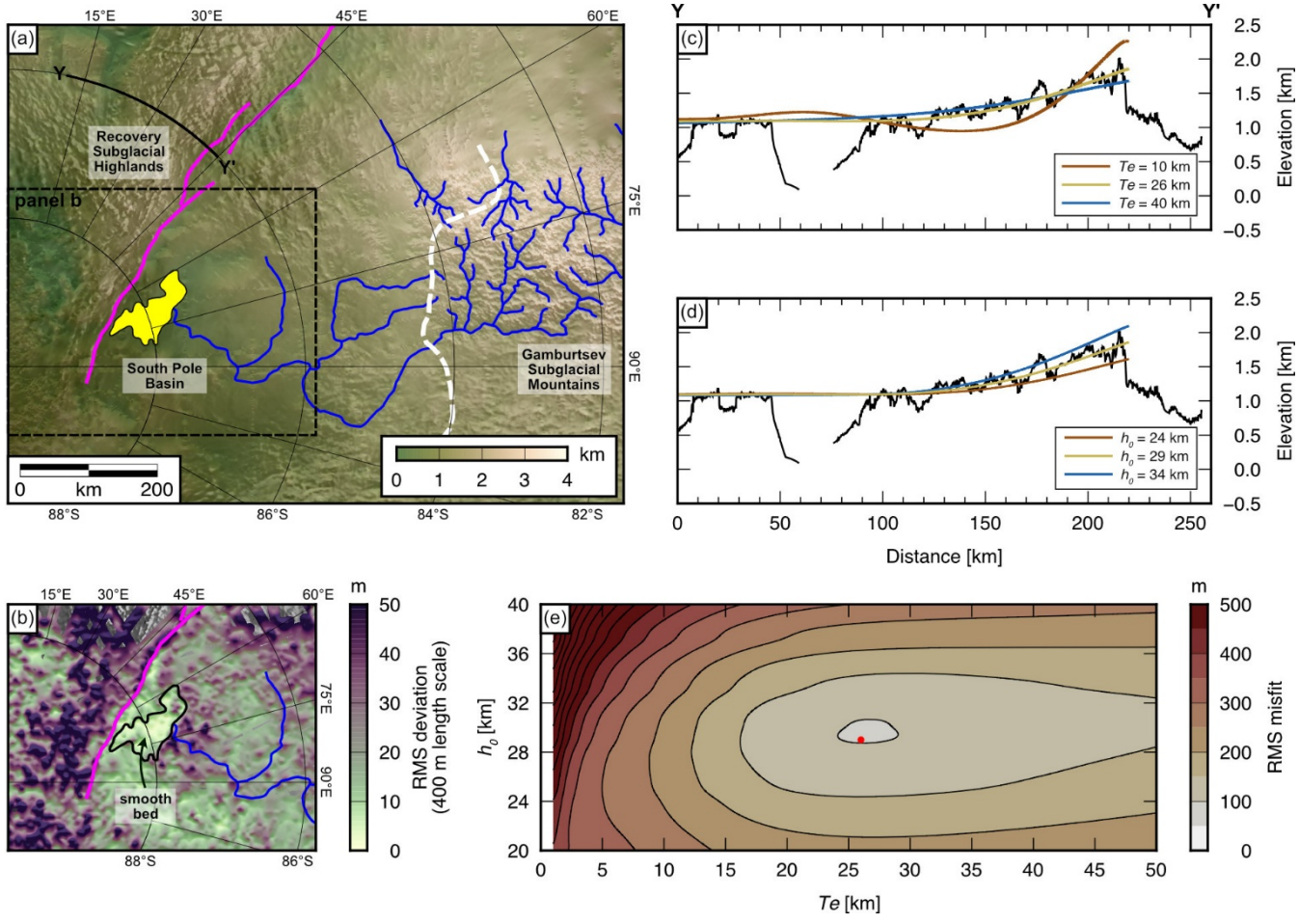

Figure 9: Potential base level for the southern GSM. (a) Relationship between the GSM valley network (blue), South Pole Basin (SPB), and the Recovery Subglacial Highlands (RSH) fault system (purple). White dashed line marks the geological boundary inferred from longitudinal profile analysis and magnetic anomalies (Fig. 5). Dashed black box marks the extent of panel b. (b) RMS deviation of bed elevation over a 400 m length scale within the SPB and RSH (Young et al., 2025). The area marked by the black outline (filled yellow in panel a) has a smooth bed (RMS deviations <10 m). (c) Flexural modelling of bed topography along profile Y–Y'. Black line is bed elevation isostatically adjusted for the removal of the present-day ice-sheet load (Paxman et al., 2022). Coloured lines show the flexural uplift profiles computed using a 1D broken elastic plate model. Flexure is caused by a combination of erosional unloading and mechanical unloading along a normal fault system (Fig. S7). Profiles are shown for three effective elastic thickness (*Te*) values, with a faulted layer thickness (h_0) of 29 km. (d) As for panel c, except coloured profiles are shown for three h_0 values with a *Te* of 26 km. (e) RMS misfit between the observed and modelled topography across the RSH as a function of *Te* and h_0. Contour interval is 50 m. The red circle marks the best-fitting combination; *Te* = 26 km; h_0 = 29 km.

https://doi.org/10.5194/egusphere-2026-847
Preprint. Discussion started: 19 February 2026

5 Discussion

5.1 Fluvial landscape preservation and glacial modification

There are multiple lines of evidence from the valley longitudinal profiles indicating that the GSM landscape is consistent with primarily fluvial incision. First, the trunk valley and tributary profiles are concave-up and tributaries join smoothly at confluences. Moreover, the recovered concavity indices are consistent with those observed from subaerial fluvial systems. The m and n exponents covary (Croissant and Braun, 2014), meaning their ratio theoretically and empirically falls within a relatively narrow range of 0.3–0.7 (Smith et al., 2022); all our recovered θ values (0.50–0.61) lie within this range. Second, when plotted in χ-elevation space, the longitudinal profiles are transformed to a single straight line (or two linear segments associated with different k_{sn} values in the case of basin 10). This behaviour is diagnostic of steady-state fluvial landscapes (Perron and Royden, 2013). Exceptions include the upper reaches of basin 8 (Fig. 8c) and the lower reaches of basin 10 (Fig. 5b), which are discussed below. Third, the trunk valley and tributaries show strong collinearity in χ-elevation space (Fig. S3), as would be expected for steady-state fluvial systems (Mudd et al., 2018). These findings are supported by the ability of the SPIM to replicate the observed longitudinal profiles for a simple set-up where only the values of m, n, and K are varied between basins (or within basins in the case of K; Fig. 7, 8).

We note that some features of the longitudinal profiles are inconsistent with fluvial incision, and instead likely reflect glacial modification of the fluvial landscape. For example, several profiles show localised deviations below the 'expected' fluvial profile generated via the SPIM, particularly in the central and northern GSM (Fig. 8). These enclosed 'lows' in the longitudinal profile are typically <20 km long and <200 m deep (Fig. 8) and often coincide with tributary junctions. These observations are consistent with expectations for glacial overdeepenings, caused by localised erosion beneath convergent valley glaciers (Cook and Swift, 2012; MacGregor et al., 2000). Some longitudinal profiles also exhibit a 'stepped' morphology (see basins 8 and 9; Fig. 8). Steps are common features in glacially modified valleys (Anderson et al., 2006), although they may alternatively reflect knickpoints at lithological contacts.

We also note that the upper part of basin 8 deviates significantly from the modelled fluvial profile and the straight line in the χ-elevation plot (Fig. 8c, d). The basin exhibits steepened 'headwaters' and a gentle slope immediately below, before reaching an inflection point at ~190 profile-km where the observed profile 'rejoins' the SPIM profile and the slope becomes steeper moving downstream. These observations are consistent with the expected morphology of fluvial profiles whose upper reaches have been modified by valley glaciation (Anderson et al., 2006; Brocklehurst and Whipple, 2006; Deal and Prasicek, 2021). The elevation of the inflection point (~1500 m above sea level) gives an approximate indication of the palaeo-equilibrium line altitude, associated with efficient glacial erosion (Brocklehurst and Whipple, 2006). Moreover, the topographic 'lip' at ~190 profile-km (Fig. 8d) may represent a former ice limit.

https://doi.org/10.5194/egusphere-2026-847
Preprint. Discussion started: 19 February 2026

These findings support the argument that the fluvial landscape of the Gamburtsevs was erosively modified by mountain-scale glaciation (Rose et al., 2013), most likely prior to EAIS growth at ca. 34 Ma. Glacial modification appears to have been greater in the central and northern Gamburtsevs, which are characterised by higher elevations than the southern Gamburtsevs (Fig. 1b, 3b) and are closer to the coast, so may have experienced higher precipitation rates. Profile overdeepening on the order of a few hundred metres would have required multiple glacial-interglacial cycles to achieve, assuming typical glacial erosion rates of order 100 m/Myr (Koppes and Montgomery, 2009). However, in all basins, particularly at lower elevations, elements of the steady-state fluvial topography are well preserved. This suggests that the coalescence of a continental-scale EAIS occurred without significant erosion, and thus potentially quite rapidly, at ca. 34 Ma (Jamieson et al., 2010; Van Breedam et al., 2022), and that since then the GSM landscape has been preserved beneath slow-moving ice (contemporary surface velocities are <5 m/yr) that is frozen to the bed, with negligible erosion rates (Creyts et al., 2014; Jamieson et al., 2023). This implies that, although the EAIS has experienced retreat during past warm climate intervals (Aitken et al., 2016; Halberstadt et al., 2024; Sangiorgi et al., 2018), a cold-based, slow-moving core has continuously persisted over the GSM since its initial growth. This has likely been aided by the high elevation and roughness of the mountains, which 'pin' the overlying ice sheet and inhibit fast flow owing to high basal friction (Bingham and Siegert, 2009).

5.2 Lithological and tectonic structure of the Gamburtsevs and surrounding regions

The distribution of k_{sn} values recovered from the longitudinal profiles, combined with spatial patterns in the magnetic anomaly and its derivatives, indicate that the southern and northern margins of the GSM are likely bounded by major geological structures. In the northern GSM there is a transition in the intensity and pattern of the magnetic anomalies across a linear boundary (Fig. 6a). The position of this boundary coincides with a step-change in k_{sn} values, which are approximately twice as high for channels on the southern side of the boundary than the northern side (Fig. 6b). The observed magnetic dichotomy has previously been inferred to mark the position of a suture between geological terranes, likely originating from the assembly of Gondwana at ca. 500 Ma (Ferraccioli et al., 2011) (Fig. 10). The suture is hypothesised to separate an accretionary fold-and-thrust terrane to the south and an arc terrane to the north (Wu et al., 2023). Although a difference in k_{sn} values might also be attributable to a spatial gradient in rock uplift rate (Eq. 6), the coincidence of this abrupt k_{sn} change with the magnetic anomaly transition supports the presence of a step-change in lithology across this boundary. This is consistent with hypotheses from crustal modelling (Ferraccioli et al., 2011; Wu et al., 2023), and we note that our results further imply lower bedrock erodibilities in the central GSM than to the north of the suture.

At the southern edge of the GSM, the valleys in basin 10 appear to cross a boundary where k_{sn} decreases (moving southwards) by a factor of ~2.6 (Fig. 5b). Again, the coincidence of this step-change with a change in the frequency content of the magnetic anomaly (Fig. 5c, d, e) is consistent with the presence of a major lithological boundary. This contact appears to approximately align with the mooted boundary between the GSM and the weakly-magnetic South Pole Province, whose geology is poorly

https://doi.org/10.5194/egusphere-2026-847
Preprint. Discussion started: 19 February 2026

understood (Ferraccioli et al., 2011; Wu et al., 2023). Our findings indicate that the South Pole Province is characterised by higher bedrock erodibilities than the GSM. Although our results alone cannot be used to assign a specific lithology to the GSM or the regions to the north and south, we note that our *K* estimates (when adjusted for *m*) are at the lower end of reported values (Stock and Montgomery, 1999), corresponding to those of granitoids and metasedimentary rocks (Fig. 7c). This broad group of lithologies is common around the exposed margins of East Antarctica, including Archaean–Neoproterozoic gneisses and Neoproterozoic–Palaeozoic metasediments (Cox et al., 2023). We suggest that these lithologies are the likely composition of the Gamburtsevs and their surroundings.

South of the GSM, we propose that the RSH represent an uplifted highland block in the footwall of an extensional fault system. There are three lines of evidence to support this hypothesis. First, the eastern side of the RSH is bounded by a strikingly linear escarpment (Fig. 9, Fig. S6). Second, the topography of the RSH block is tilted away from the escarpment, as is expected for the pattern of flexural uplift due to mechanical unloading of the lithosphere in the vicinity of a normal fault (Fig. S7) (Ebinger et al., 1991; Weissel and Karner, 1989). Third, the decrease in block width and relief at the southern end of the RSH (Fig. S8) is consistent with expectations of the topography at the propagating tip of a normal fault system (Densmore et al., 2005, 2007). This evidence for southward fault tip propagation, combined with observed low-magnitude extensional earthquake events (Lough et al., 2018), implies that this fault system may have accommodated extensional deformation and triggered uplift at the southern end of the RSH as recently as the Cenozoic (before and/or after Oligocene glaciation). We hypothesise that this fault propagation may have cut off a former palaeo-fluvial (and/or -glacial) drainage pathway between the GSM and the Weddell Sea via the Pensacola-Pole Basin (Fig. 1b), which could have trapped Gamburtsev-derived sediment in the SPB (Licht and Hemming, 2017) and raised base level for the southern flank of the Gamburtsevs (Fig. 10).

Deeper crustal and lithosphere structure also has important implications for ice-sheet dynamics. The best-fitting faulted layer thickness of 29 km (Fig. 9d) is in good agreement with estimates from East Africa, which is associated with a thicker brittle crustal layer (25–30 km) than many rifts due to inherited thick cratonic lithosphere and/or low heat flow (Lavier and Buck, 2002). Earthquake events in this part of East Antarctica are located at depths of up to 30 km beneath the ice surface (Lough et al., 2018), supporting the presence of a thick brittle crust. This suggests that this part of the East Antarctic interior is associated with thick lithosphere and low heat flow, as is inferred from seismic tomographic analysis (Hazzard et al., 2023).

To the east of the RSH, the hanging-wall topography of the South Pole Basin is lower-lying and less rugged (Fig. 9). Within the SPB is a particularly smooth, flat-lying, topographically enclosed region (Fig. 9b) with an area of ~4800 km^2. This is comparable in size to the Great Salt Lake (Utah, USA), which is similarly situated in the hanging wall of a major range-bounding normal fault system in a continental interior. Given these observations and the fact that the valley network originating in the southern GSM appears to terminate at this location (Fig. 9), we propose that this smooth basin: (i) likely formed due to subsidence of the hanging-wall of the RSH fault system, (ii) may have been endorheic and constituted the local base level for the southern GSM if it existed prior to glaciation, and (iii) likely contains sedimentary material transported from the Gamburtsevs by river systems prior to ca. 34 Ma. We acknowledge the possibility that further sediment deposition within the

https://doi.org/10.5194/egusphere-2026-847
Preprint. Discussion started: 19 February 2026

basin may have occurred subglacially (Young et al., 2025) but, given the lack of evidence for any major change in regional palaeotopographic configuration since glaciation (Paxman, 2023), this would have been a natural area for pre-glacial sediment accumulation in the East Antarctic interior (Fig. 10). We propose that this smooth region, situated beneath ~3.5 km of ice, could be a promising target for sub-ice drilling programmes with the ambition of recovering detrital sedimentary material sourced from the southern GSM. Analysis of such material would potentially provide important constraints on East Antarctic uplift and erosion histories, lithology and sediment provenance, palaeoclimate, and the nature of early glaciation.

5.3 Timing of Gamburtsev uplift

In this section we explore the extent to which stream power incision modelling enables constraints to be placed on the age of the fluvial landscape, which would in turn constrain the timing of Gamburtsev uplift. We emphasise that the SPIM is inherently underconstrained, especially given the ambiguity regarding long-term erosion rates in interior East Antarctica, making a precise reconstruction of uplift history impossible without further constraints. We instead ask whether, for a plausible parameter space, we can place realistic bounds on uplift history and compare this to existing hypotheses for GSM evolution.

For the end-member K values tested in our longitudinal profile modelling, which correspond to the plausible range of pre-glacial denudation rates for the Gamburtsevs (see section 3.3), we found best-fitting model run times of 22–216 Myr for basin 10 (Fig. 7). If fluvial erosion was 'switched off' following EAIS growth at ca. 34 Ma, the implied age range for the commencement of GSM uplift is ca. 250 to 56 Ma. Thermochronological evidence from the Transantarctic Mountains and the Lambert Glacier-Prydz Bay region, using detrital material that may have been eroded from the continental interior of East Antarctica including the GSM, records four regional tectonic / magmatic / exhumation events in the Phanerozoic (Fitzgerald and Goodge, 2022; Thomson et al., 2013) that represent candidate intervals for GSM uplift:

(1) Cambro-Ordovician (ca. 550–450 Ma) metamorphism, magmatism and subsequent cooling occurred in relation to collisional orogeny during Gondwana assembly (Fitzgerald and Goodge, 2022; Thomson et al., 2013). Our results preclude any model in which GSM uplift occurred solely at this time (An et al., 2015; Van De Flierdt et al., 2008). Uplift of an 'ancestral' Gamburtsev mountain range in the early Palaeozoic is possible (Fitzgerald and Goodge, 2022) — and the geological boundaries recorded by the channel steepness indices likely reflect this amalgamation (Ferraccioli et al., 2011; Wu et al., 2023) — but subsequent denudation followed by renewed uplift at some point after ca. 250 Ma would be necessary.

(2) Permo-Triassic (ca. 250 Ma) cooling and exhumation was potentially related to intra-continental rifting, which has been hypothesised to have been a trigger for GSM uplift (Ferraccioli et al., 2011; Phillips and Läufer, 2009; Thomson et al., 2013). The timing of this event is at the uppermost limit of our feasible age range, meaning it would necessitate markedly low erosion rates (~10 m/Myr) after ca. 250 Ma to have been the primary cause of GSM uplift. We deem such erosion rates to be highly unlikely for the Gamburtsevs for the reasons given in section 3.3.

https://doi.org/10.5194/egusphere-2026-847
Preprint. Discussion started: 19 February 2026

(3) Early Jurassic (ca. 180 Ma) cooling is observed in some Transantarctic Mountain samples and has been interpreted as evidence of exhumation accompanying extension during the breakup of Gondwana (Fitzgerald and Goodge, 2022).

(4) Cooling and exhumation in the mid-Cretaceous (ca. 125–90 Ma) may have been related to reactivation of the East Antarctic Rift System to accommodate interior transtensional deformation (Ferraccioli et al., 2011; Fitzgerald and Goodge, 2022; Phillips and Läufer, 2009; Thomson et al., 2013).

If the third and/or fourth events were primarily responsible for GSM uplift, the implied subsequent long-term erosion rate would be up to 40 m/Myr, which is more consistent with orogens resembling the GSM (Fig. 7b). We therefore propose that the fluvial incision preserved in the landscape of the GSM most likely occurred in response to uplift that commenced in the Jurassic and/or Cretaceous periods (Fig. 10). If this is correct, we may expect topographic structures indicative of extensional and/or later transtensional deformation to be preserved in the regions surrounding the GSM, which remain poorly surveyed by radio-echo sounding. Future mapping and analysis of topographic lineaments and the planform patterns of sub-ice valley networks and drainage basins (Mudd et al., 2022), using improved techniques for mapping the texture of the bed topography (Ockenden et al., 2026), could enable this hypothesis to be tested in the future.

Finally, we note that the presence of knickpoints in the lower reaches of basin 10 means that a proportion of the uplift may have occurred a relatively short amount of time before glaciation at ca. 34 Ma. We can discount these features arising due to glacial modification of the valley profile because they are situated >700 km downstream of the profile 'headwaters' and well downstream of the reconstructed limit of late Eocene mountain-scale glaciation (Rose et al., 2013), and because the observed profile upstream of the knickpoints is well fit by the concave-up SPIM profile (Fig. 7a). There are three other scenarios that may explain the presence of these knickpoints (Lague, 2014): (i) static knickpoints due to a change in lithology (leading to spatial variation in K), (ii) static knickpoints due to the presence of faults (spatial variation in U), or (iii) upstream-propagating knickpoints due to base-level fall (temporal variation in U).

Although there is no obvious magnetic anomaly transition associated with the knickpoints, there is insufficient evidence to definitively rule out any of these scenarios. In the scenario where the knickpoints are transient features arising from rock uplift or base-level fall and concomitant incision, their combined 'relief' constrains the amount of base-level fall (over two phases) to ~470 m. Based on Eq. (13), the upper limit for the time for the upper knickpoint to propagate upstream to its observed position (assuming the mapped profile starts at base level) is 18 Myr. If fluvial incision were 'switched off' at ca. 34 Ma, this implies that the base level fall occurred between 52 and 34 Ma. Base-level fall may have been caused by subsidence in the vicinity of the SPB (e.g., due to extensional fault activity; see section 5.2), uplift of the GSM, or both (Fig. 10). If such an event did occur, its timing may have had important implications for the nature and timing of Antarctic glacial inception. For a standard environmental lapse rate of ~6.5 °C/km, uplift of ~470 m would decrease surface temperatures over the tops of the mountains by ~3–4 °C, potentially enabling the onset of alpine glaciation and triggering the series of ice-sheet-climate feedbacks that paved the way for EAIS growth at ca. 34 Ma (DeConto and Pollard, 2003) (Fig. 10).

https://doi.org/10.5194/egusphere-2026-847
Preprint. Discussion started: 19 February 2026

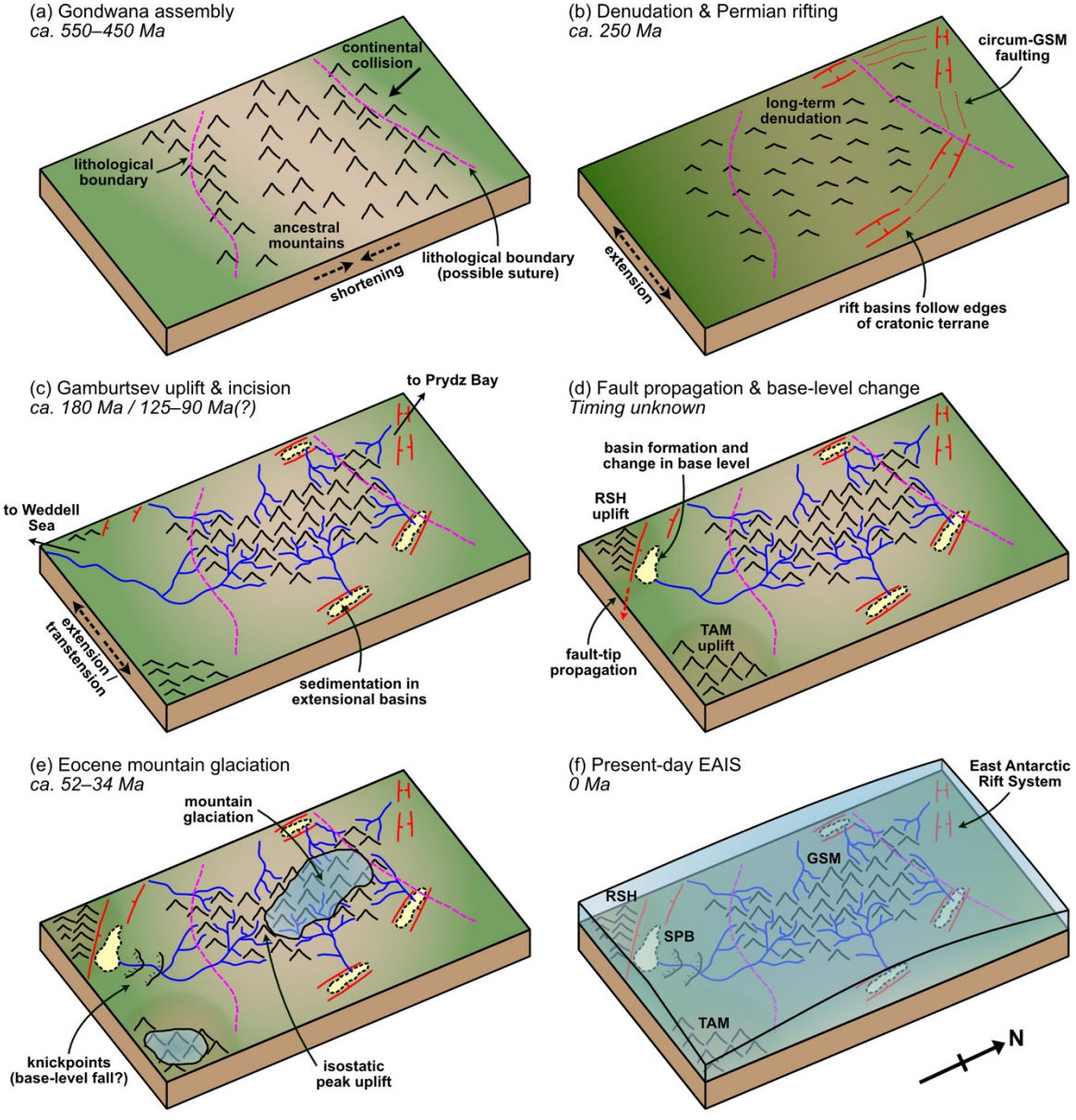

Figure 10: Schematic inferred long-term landscape evolution of the Gamburtsev region. (a) Continental collision and orogenesis in the Cambro-Ordovician resulted in Gondwana assembly and the formation of major lithological boundaries / sutures. (b) Subsequent long-term denudation reduced the relief of interior East Antarctica. Permian extensional deformation resulted in the formation of the East Antarctic Rift System (red lines), which likely exploited more mobile belts around ancient cratonic terranes and may have been responsible for formation of the contemporary Gamburtsevs, although this would require very low pre-glacial erosion rates (see text). (c) Uplift of the contemporary Gamburtsevs likely commenced in the Jurassic / Cretaceous. River networks incised the mountains and deposited sediments in the interior extensional basins as well as routing material to Prydz Bay to the north and the Weddell Sea to the south. (d) The fault system bounding the RSH propagated towards the South Pole, potentially cutting off the drainage pathway to the Weddell Sea and forming an interior depocentre in the SPB. (e) Base-level fall prior to glaciation may have been responsible for the formation of two knickpoints upstream of the SPB. Mountain glaciation commenced on the high terrain of the GSM and Transantarctic Mountains (TAM) and valley incision drove isostatic peak uplift. (f) The EAIS rapidly expanded and preserved the subglacial landscape due to negligible erosion rates.

https://doi.org/10.5194/egusphere-2026-847
Preprint. Discussion started: 19 February 2026

6 Conclusions

In this study, we have analysed valley longitudinal profiles from the Gamburtsev Subglacial Mountains, East Antarctica. Our aim was to shed light on sub-ice lithological composition, the tectonic and surface processes that have shaped the regional topography, and the timing of valley incision. Based on our findings, we conclude the following:

1. The Gamburtsev valley longitudinal profiles are primarily consistent with a steady-state fluvial landscape that evolved prior to glaciation and has been preserved since EAIS growth at ca. 34 Ma, with minor localised modification by early mountain ice fields and glaciers.
2. Channel steepness indices and magnetic anomalies suggest that major geological boundaries are present at the northern and southern edges of the Gamburtsevs, with the lowest bedrock erodibilities found within the core of the mountain range. This demonstrates the potential for preserved valley longitudinal profiles to record variations in sub-ice geology.
3. Stream power incision modelling suggests that uplift of the Gamburtsevs and incision of the fluvial landscape commenced no earlier than the Permo-Triassic (ca. 250 Ma) and was likely substantially younger. We suggest that a substantial component of GSM uplift likely occurred in the Jurassic and/or Cretaceous (ca. 180–90 Ma).
4. Material eroded from the southern Gamburtsevs was transported towards a base level near the South Pole, where sediments derived from the mountains may be preserved in interior depocentres formed due to extensional faulting. The South Pole Basin may be a promising target for recovery of detrital sedimentary material sourced from the southern GSM via future sub-ice drilling.

Data/Code availability

Datasets generated in this study are available at the following Zenodo repository: https://doi.org/10.5281/zenodo.18620873. The radio-echo sounding ice thickness and bed pick data used in this study are available via the following repositories:

- AGAP: https://doi.org/10/gzqw (Ferraccioli et al., 2011) and https://doi.org/10.1594/IEDA/313685 (Bell et al., 2011)
- PolarGAP: https://doi.org/10/g7qp (Paxman et al., 2019; Winter et al., 2018)
- Operation IceBridge: https://doi.org/10.5067/GDQ0CUCVTE2Q (MacGregor et al., 2021)
- COLDEX: https://www.openpolarradar.org (Young et al., 2025)

The Bedmap3 digital elevation model is a publicly available dataset found at: https://doi.org/10.5285/2d0e4791-8e20-46a3-80e4-f5f6716025d2 (Pritchard et al., 2025). The ADMAP-2B magnetic anomaly compilation is a publicly available dataset found at: https://doi.org/10.1594/PANGAEA.965433 (Eagles et al., 2024; Golynsky et al., 2018). The source code for the stream power incision model was accessed from the GitHub repository: https://github.com/BCampforts/SPLM (Campforts et al., 2017).

https://doi.org/10.5194/egusphere-2026-847
Preprint. Discussion started: 19 February 2026

Acknowledgements

GJGP was supported by a Royal Society University Research Fellowship (award number URF\R1\241308). We acknowledge the contributions of all the scientific and technical staff involved in the acquisition and processing of the airborne radio-echo sounding and magnetic data used in this paper. We also thank Andy Wickert for helpful discussions during the early development of the manuscript. This research is a contribution to the Scientific Committee on Antarctic Research (SCAR) Instabilities and Thresholds in Antarctica (INSTANT) programme and its Antarctic Geological Boundary Conditions (ABC) sub-committee. Hydrological calculations were performed using TopoToolbox version 3.0 (Schwanghart and Scherler, 2014). Figures were prepared using the Generic Mapping Tools (GMT) version 6.6 (Wessel et al., 2019) and colour palettes from Scientific Colour Maps version 8.0 (Crameri et al., 2020).

Author contributions

GJGP: conceptualisation, methodology, investigation, visualisation, writing (original draft preparation). FJC: conceptualisation, methodology, writing (review and editing), SSRJ: conceptualisation, writing (review and editing), ALD: conceptualisation, writing (review and editing).

Competing interests

FJC is a member of the editorial board of Earth Surface Dynamics.

References

Aitken, A. R. A., Roberts, J. L., Ommen, T. D. V., Young, D. A., Golledge, N. R., Greenbaum, J. S., Blankenship, D. D., and Siegert, M. J.: Repeated large-scale retreat and advance of Totten Glacier indicated by inland bed erosion, Nature, 533, 385–389, https://doi.org/10.1038/nature17447, 2016.

An, M., Wiens, D. A., Zhao, Y., Feng, M., Nyblade, A. A., Kanao, M., Li, Y., Maggi, A., and Lévêque, J.: S-velocity model and inferred Moho topography beneath the Antarctic Plate from Rayleigh waves, JGR Solid Earth, 120, 359–383, https://doi.org/10.1002/2014JB011332, 2015.

Anderson, R. S., Molnar, P., and Kessler, M. A.: Features of glacial valley profiles simply explained, J. Geophys. Res., 111, 2005JF000344, https://doi.org/10.1029/2005JF000344, 2006.

Bell, R. E., Ferraccioli, F., Creyts, T. T., Braaten, D., Corr, H., Das, I., Damaske, D., Frearson, N., Jordan, T., Rose, K., Studinger, M., and Wolovick, M.: Widespread Persistent Thickening of the East Antarctic Ice Sheet by Freezing from the Base, Science, 331, 1592–1595, https://doi.org/10.1126/science.1200109, 2011.

Bingham, R. G. and Siegert, M. J.: Quantifying subglacial bed roughness in Antarctica: implications for ice-sheet dynamics and history, Quaternary Science Reviews, 28, 223–236, https://doi.org/10.1016/j.quascirev.2008.10.014, 2009.

Bo, S., Siegert, M. J., Mudd, S. M., Sugden, D., Fujita, S., Xiangbin, C., Yunyun, J., Xueyuan, T., and Yuansheng, L.: The Gamburtsev mountains and the origin and early evolution of the Antarctic Ice Sheet, Nature, 459, 690–693, https://doi.org/10.1038/nature08024, 2009.

Brocklehurst, S. H. and Whipple, K. X.: Assessing the relative efficiency of fluvial and glacial erosion through simulation of fluvial landscapes, Geomorphology, 75, 283–299, https://doi.org/10.1016/j.geomorph.2005.07.028, 2006.

Campforts, B. and Govers, G.: Keeping the edge: A numerical method that avoids knickpoint smearing when solving the stream power law, JGR Earth Surface, 120, 1189–1205, https://doi.org/10.1002/2014JF003376, 2015.

Campforts, B., Schwanghart, W., and Govers, G.: Accurate simulation of transient landscape evolution by eliminating numerical diffusion: the TTLEM 1.0 model, Earth Surf. Dynam., 5, 47–66, https://doi.org/10.5194/esurf-5-47-2017, 2017.

Chang, M., Jamieson, S. S. R., Bentley, M. J., and Stokes, C. R.: The surficial and subglacial geomorphology of western Dronning Maud Land, Antarctica, Journal of Maps, 12, 892–903, https://doi.org/10.1080/17445647.2015.1097289, 2016.

Contreras-Reyes, E. and Osses, A.: Lithospheric flexure modelling seaward of the Chile trench: implications for oceanic plate weakening in the Trench Outer Rise region: Outer-rise flexure modelling off Chile, Geophysical Journal International, 182, 97–112, https://doi.org/10.1111/j.1365-246X.2010.04629.x, 2010.

Cook, S. J. and Swift, D. A.: Subglacial basins: Their origin and importance in glacial systems and landscapes, Earth-Science Reviews, 115, 332–372, https://doi.org/10.1016/j.earscirev.2012.09.009, 2012.

Cox, S. C., Smith Lyttle, B., Elkind, S., Smith Siddoway, C., Morin, P., Capponi, G., Abu-Alam, T., Ballinger, M., Bamber, L., Kitchener, B., Lelli, L., Mawson, J., Millikin, A., Dal Seno, N., Whitburn, L., White, T., Burton-Johnson, A., Crispini, L., Elliot, D., Elvevold, S., Goodge, J., Halpin, J., Jacobs, J., Martin, A. P., Mikhalsky, E., Morgan, F., Scadden, P., Smellie, J., and Wilson, G.: A continent-wide detailed geological map dataset of Antarctica, Sci Data, 10, 250, https://doi.org/10.1038/s41597-023-02152-9, 2023.

Coxall, H. K., Wilson, P. A., Pälike, H., Lear, C. H., and Backman, J.: Rapid stepwise onset of Antarctic glaciation and deeper calcite compensation in the Pacific Ocean, Nature, 433, 53–57, https://doi.org/10.1038/nature03135, 2005.

Crameri, F., Shephard, G. E., and Heron, P. J.: The misuse of colour in science communication, Nat Commun, 11, 5444, https://doi.org/10.1038/s41467-020-19160-7, 2020.

Creyts, T. T., Ferraccioli, F., Bell, R. E., Wolovick, M., Corr, H., Rose, K. C., Frearson, N., Damaske, D., Jordan, T., Braaten, D., and Finn, C.: Freezing of ridges and water networks preserves the Gamburtsev Subglacial Mountains for millions of years, Geophysical Research Letters, 41, 8114–8122, https://doi.org/10.1002/2014GL061491, 2014.

Croissant, T. and Braun, J.: Constraining the stream power law: a novel approach combining a landscape evolution model and an inversion method, Earth Surf. Dynam., 2, 155–166, https://doi.org/10.5194/esurf-2-155-2014, 2014.

Deal, E. and Prasicek, G.: The Sliding Ice Incision Model: A New Approach to Understanding Glacial Landscape Evolution, Geophysical Research Letters, 48, e2020GL089263, https://doi.org/10.1029/2020GL089263, 2021.

DeConto, R. M. and Pollard, D.: Rapid Cenozoic glaciation of Antarctica induced by declining atmospheric CO2, Nature, 421, 245–249, https://doi.org/10.1038/nature01290, 2003.

https://doi.org/10.5194/egusphere-2026-847
Preprint. Discussion started: 19 February 2026

Demoulin, A., Beckers, A., and Hubert-Ferrari, A.: Patterns of Quaternary uplift of the Corinth rift southern border (N Peloponnese, Greece) revealed by fluvial landscape morphometry, Geomorphology, 246, 188–204, https://doi.org/10.1016/j.geomorph.2015.05.032, 2015.

Densmore, A. L., Dawers, N. H., Gupta, S., and Guidon, R.: What sets topographic relief in extensional footwalls?, Geol, 33, 453, https://doi.org/10.1130/G21440.1, 2005.

Densmore, A. L., Gupta, S., Allen, P. A., and Dawers, N. H.: Transient landscapes at fault tips, J. Geophys. Res., 112, 2006JF000560, https://doi.org/10.1029/2006JF000560, 2007.

Duvall, A., Kirby, E., and Burbank, D.: Tectonic and lithologic controls on bedrock channel profiles and processes in coastal California, J. Geophys. Res., 109, 2003JF000086, https://doi.org/10.1029/2003JF000086, 2004.

Eagles, G., Golynsky, A. V., Kim, H. R., Paxman, G. J. G., and Ferraccioli, F.: ADMAP's Antarctic magnetic anomaly grids transformed for use with open source software, https://doi.org/10.1594/PANGAEA.965433, 2024.

Ebinger, C. J., Karner, G. D., and Weissel, J. K.: Mechanical strength of extended continental lithosphere: Constraints from the Western Rift System, East Africa, Tectonics, 10, 1239–1256, https://doi.org/10.1029/91TC00579, 1991.

Ferraccioli, F., Finn, C. A., Jordan, T. A., Bell, R. E., Anderson, L. M., and Damaske, D.: East Antarctic rifting triggers uplift of the Gamburtsev Mountains, Nature, 479, 388–392, https://doi.org/10.1038/nature10566, 2011.

Fitzgerald, P. G. and Goodge, J. W.: Exhumation and tectonic history of inaccessible subglacial interior East Antarctica from thermochronology on glacial erratics, Nat Commun, 13, 6217, https://doi.org/10.1038/s41467-022-33791-y, 2022.

Flint, J. J.: Stream gradient as a function of order, magnitude, and discharge, Water Resources Research, 10, 969–973, https://doi.org/10.1029/WR010i005p00969, 1974.

Frémand, A. C., Bodart, J. A., Jordan, T. A., Ferraccioli, F., Robinson, C., Corr, H. F. J., Peat, H. J., Bingham, R. G., and Vaughan, D. G.: British Antarctic Survey's aerogeophysical data: releasing 25 years of airborne gravity, magnetic, and radar datasets over Antarctica, Earth Syst. Sci. Data, 14, 3379–3410, https://doi.org/10.5194/essd-14-3379-2022, 2022.

Golynsky, A. V., Ferraccioli, F., Hong, J. K., Golynsky, D. A., Von Frese, R. R. B., Young, D. A., Blankenship, D. D., Holt, J. W., Ivanov, S. V., Kiselev, A. V., Masolov, V. N., Eagles, G., Gohl, K., Jokat, W., Damaske, D., Finn, C., Aitken, A., Bell, R. E., Armadillo, E., Jordan, T. A., Greenbaum, J. S., Bozzo, E., Caneva, G., Forsberg, R., Ghidella, M., Galindo-Zaldivar, J., Bohoyo, F., Martos, Y. M., Nogi, Y., Quartini, E., Kim, H. R., and Roberts, J. L.: New Magnetic Anomaly Map of the Antarctic, Geophysical Research Letters, 45, 6437–6449, https://doi.org/10.1029/2018GL078153, 2018.

Goren, L., Fox, M., and Willett, S. D.: Tectonics from fluvial topography using formal linear inversion: Theory and applications to the Inyo Mountains, California, JGR Earth Surface, 119, 1651–1681, https://doi.org/10.1002/2014JF003079, 2014.

Gulick, S. P. S., Shevenell, A. E., Montelli, A., Fernandez, R., Smith, C., Warny, S., Bohaty, S. M., Sjunneskog, C., Leventer, A., Frederick, B., and Blankenship, D. D.: Initiation and long-term instability of the East Antarctic Ice Sheet, Nature, 552, 225–229, https://doi.org/10.1038/nature25026, 2017.

Halberstadt, A. R. W., Gasson, E., Pollard, D., Marschalek, J., and DeConto, R. M.: Geologically constrained 2-million-year-long simulations of Antarctic Ice Sheet retreat and expansion through the Pliocene, Nat Commun, 15, 7014, https://doi.org/10.1038/s41467-024-51205-z, 2024.

https://doi.org/10.5194/egusphere-2026-847
Preprint. Discussion started: 19 February 2026

Hazzard, J. A. N., Richards, F. D., Goes, S. D. B., and Roberts, G. G.: Probabilistic Assessment of Antarctic Thermomechanical Structure: Impacts on Ice Sheet Stability, JGR Solid Earth, 128, e2023JB026653, https://doi.org/10.1029/2023JB026653, 2023.

Hergarten, S., Robl, J., and Stüwe, K.: Tectonic geomorphology at small catchment sizes – extensions of the stream-power approach and the χ method, Earth Surf. Dynam., 4, 1–9, https://doi.org/10.5194/esurf-4-1-2016, 2016.

Hönisch, B., Royer, D. L., Breecker, D. O., Polissar, P. J., Bowen, G. J., Henehan, M. J., Cui, Y., Steinthorsdottir, M., McElwain, J. C., Kohn, M. J., Pearson, A., Phelps, S. R., Uno, K. T., Ridgwell, A., Anagnostou, E., Austermann, J., Badger, M. P. S., Barclay, R. S., Bijl, P. K., Chalk, T. B., Scotese, C. R., De La Vega, E., DeConto, R. M., Dyez, K. A., Ferrini, V., Franks, P. J., Giulivi, C. F., Gutjahr, M., Harper, D. T., Haynes, L. L., Huber, M., Snell, K. E., Keisling, B. A., Konrad, W., Lowenstein, T. K., Malinverno, A., Guillermic, M., Mejía, L. M., Milligan, J. N., Morton, J. J., Nordt, L., Whiteford, R., Roth-Nebelsick, A., Rugenstein, J. K. C., Schaller, M. F., Sheldon, N. D., Sosdian, S., Wilkes, E. B., Witkowski, C. R., Zhang, Y. G., Anderson, L., Beerling, D. J., Bolton, C., Cerling, T. E., Cotton, J. M., Da, J., Ekart, D. D., Foster, G. L., Greenwood, D. R., Hyland, E. G., Jagniecki, E. A., Jasper, J. P., Kowalczyk, J. B., Kunzmann, L., Kürschner, W. M., Lawrence, C. E., Lear, C. H., Martínez-Botí, M. A., Maxbauer, D. P., Montagna, P., Naafs, B. D. A., Rae, J. W. B., Raitzsch, M., Retallack, G. J., Ring, S. J., Seki, O., Sepúlveda, J., Sinha, A., Tesfamichael, T. F., Tripati, A., Van Der Burgh, J., Yu, J., Zachos, J. C., and Zhang, L.: Toward a Cenozoic history of atmospheric CO_2, Science, 382, eadi5177, https://doi.org/10.1126/science.adi5177, 2023.

Howard, A. D.: A detachment-limited model of drainage basin evolution, Water Resources Research, 30, 2261–2285, https://doi.org/10.1029/94WR00757, 1994.

Howard, A. D. and Kerby, G.: Channel changes in badlands, Geol Soc America Bull, 94, 739, https://doi.org/10.1130/0016-7606(1983)94%253C739:CCIB%253E2.0.CO;2, 1983.

Howat, I. M., Porter, C., Smith, B. E., Noh, M.-J., and Morin, P.: The Reference Elevation Model of Antarctica, The Cryosphere, 13, 665–674, https://doi.org/10.5194/tc-13-665-2019, 2019.

Jamieson, S. S. R., Hulton, N. R. J., Sugden, D. E., Payne, A. J., and Taylor, J.: Cenozoic landscape evolution of the Lambert basin, East Antarctica: the relative role of rivers and ice sheets, Global and Planetary Change, 45, 35–49, https://doi.org/10.1016/j.gloplacha.2004.09.015, 2005.

Jamieson, S. S. R., Sugden, D. E., and Hulton, N. R. J.: The evolution of the subglacial landscape of Antarctica, Earth and Planetary Science Letters, 293, 1–27, https://doi.org/10.1016/j.epsl.2010.02.012, 2010.

Jamieson, S. S. R., Ross, N., Paxman, G. J. G., Clubb, F. J., Young, D. A., Yan, S., Greenbaum, J., Blankenship, D. D., and Siegert, M. J.: An ancient river landscape preserved beneath the East Antarctic Ice Sheet, Nat Commun, 14, 6507, https://doi.org/10.1038/s41467-023-42152-2, 2023.

Jezek, K., Curlander, J., Carsey, F., Wales, C., and Barry, R.: RAMP AMM-1 SAR Image Mosaic of Antarctica, Version 2, https://doi.org/10.5067/8AF4ZRPULS4H, 2013.

Koppes, M. N. and Montgomery, D. R.: The relative efficacy of fluvial and glacial erosion over modern to orogenic timescales, Nature Geosci, 2, 644–647, https://doi.org/10.1038/ngeo616, 2009.

Lague, D.: The stream power river incision model: evidence, theory and beyond, Earth Surf Processes Landf, 39, 38–61, https://doi.org/10.1002/esp.3462, 2014.

https://doi.org/10.5194/egusphere-2026-847
Preprint. Discussion started: 19 February 2026

Lavier, L. L. and Buck, W. R.: Half graben versus large-offset low-angle normal fault: Importance of keeping cool during normal faulting, J.-Geophys.-Res., 107, https://doi.org/10.1029/2001JB000513, 2002.

Licht, K. J. and Hemming, S. R.: Analysis of Antarctic glacigenic sediment provenance through geochemical and petrologic applications, Quaternary Science Reviews, 164, 1–24, https://doi.org/10.1016/j.quascirev.2017.03.009, 2017.

Lough, A. C., Wiens, D. A., and Nyblade, A.: Reactivation of ancient Antarctic rift zones by intraplate seismicity, Nature Geosci, 11, 515–519, https://doi.org/10.1038/s41561-018-0140-6, 2018.

MacGregor, J. A., Boisvert, L. N., Medley, B., Petty, A. A., Harbeck, J. P., Bell, R. E., Blair, J. B., Blanchard-Wrigglesworth, E., Buckley, E. M., Christoffersen, M. S., Cochran, J. R., Csathó, B. M., De Marco, E. L., Dominguez, R. T., Fahnestock, M. A., Farrell, S. L., Gogineni, S. P., Greenbaum, J. S., Hansen, C. M., Hofton, M. A., Holt, J. W., Jezek, K. C., Koenig, L. S., Kurtz, N. T., Kwok, R., Larsen, C. F., Leuschen, C. J., Locke, C. D., Manizade, S. S., Martin, S., Neumann, T. A., Nowicki, S. M. J., Paden, J. D., Richter-Menge, J. A., Rignot, E. J., Rodríguez-Morales, F., Siegfried, M. R., Smith, B. E., Sonntag, J. G., Studinger, M., Tinto, K. J., Truffer, M., Wagner, T. P., Woods, J. E., Young, D. A., and Yungel, J. K.: The Scientific Legacy of NASA's Operation IceBridge, Reviews of Geophysics, 59, e2020RG000712, https://doi.org/10.1029/2020RG000712, 2021.

MacGregor, K. R., Anderson, R. S., Anderson, S. P., and Waddington, E. D.: Numerical simulations of glacial-valley longitudinal profile evolution, Geol, 28, 1031, https://doi.org/10.1130/0091-7613(2000)28%253C1031:NSOGLP%253E2.0.CO;2, 2000.

Mudd, S. M., Attal, M., Milodowski, D. T., Grieve, S. W. D., and Valters, D. A.: A statistical framework to quantify spatial variation in channel gradients using the integral method of channel profile analysis, JGR Earth Surface, 119, 138–152, https://doi.org/10.1002/2013JF002981, 2014.

Mudd, S. M., Clubb, F. J., Gailleton, B., and Hurst, M. D.: How concave are river channels?, Earth Surf. Dynam., 6, 505–523, https://doi.org/10.5194/esurf-6-505-2018, 2018.

Mudd, S. M., Roda-Boluda, D. C., Goren, L., and Clubb, F. J.: Beyond the Long Profile, in: Treatise on Geomorphology, Elsevier, 22–52, https://doi.org/10.1016/B978-0-12-818234-5.00026-2, 2022.

Ockenden, H., Bingham, R. G., Goldberg, D., Curtis, A., and Morlighem, M.: Complex mesoscale landscapes beneath Antarctica mapped from space, Science, 391, 314–319, https://doi.org/10.1126/science.ady2532, 2026.

Paxman, G. J. G.: Antarctic palaeotopography, Memoirs, 56, 231–251, https://doi.org/10.1144/M56-2020-7, 2023.

Paxman, G. J. G., Watts, A. B., Ferraccioli, F., Jordan, T. A., Bell, R. E., Jamieson, S. S. R., and Finn, C. A.: Erosion-driven uplift in the Gamburtsev Subglacial Mountains of East Antarctica, Earth and Planetary Science Letters, 452, 1–14, https://doi.org/10.1016/j.epsl.2016.07.040, 2016.

Paxman, G. J. G., Jamieson, S. S. R., Ferraccioli, F., Jordan, T. A., Bentley, M. J., Ross, N., Forsberg, R., Matsuoka, K., Steinhage, D., Eagles, G., and Casal, T. G.: Subglacial Geology and Geomorphology of the Pensacola-Pole Basin, East Antarctica, Geochem Geophys Geosyst, 20, 2786–2807, https://doi.org/10.1029/2018GC008126, 2019.

Paxman, G. J. G., Austermann, J., and Hollyday, A.: Total isostatic response to the complete unloading of the Greenland and Antarctic Ice Sheets, Sci Rep, 12, 11399, https://doi.org/10.1038/s41598-022-15440-y, 2022.

Perron, J. T. and Royden, L.: An integral approach to bedrock river profile analysis, Earth Surf Processes Landf, 38, 570–576, https://doi.org/10.1002/esp.3302, 2013.

https://doi.org/10.5194/egusphere-2026-847
Preprint. Discussion started: 19 February 2026

Phillips, G. and Läufer, A. L.: Brittle deformation relating to the Carboniferous–Cretaceous evolution of the Lambert Graben, East Antarctica: A precursor for Cenozoic relief development in an intraplate and glaciated region, Tectonophysics, 471, 216–224, https://doi.org/10.1016/j.tecto.2009.02.012, 2009.

Portenga, E. W. and Bierman, P. R.: Understanding Earth's eroding surface with 10Be, GSAT, 21, 4–10, https://doi.org/10.1130/G111A.1, 2011.

Pritchard, H. D., Fretwell, P. T., Fremand, A. C., Bodart, J. A., Kirkham, J. D., Aitken, A., Bamber, J., Bell, R., Bianchi, C., Bingham, R. G., Blankenship, D. D., Casassa, G., Christianson, K., Conway, H., Corr, H. F. J., Cui, X., Damaske, D., Damm, V., Dorschel, B., Drews, R., Eagles, G., Eisen, O., Eisermann, H., Ferraccioli, F., Field, E., Forsberg, R., Franke, S., Goel, V., Gogineni, S. P., Greenbaum, J., Hills, B., Hindmarsh, R. C. A., Hoffman, A. O., Holschuh, N., Holt, J. W., Humbert, A., Jacobel, R. W., Jansen, D., Jenkins, A., Jokat, W., Jong, L., Jordan, T. A., King, E. C., Kohler, J., Krabill, W., Maton, J., Gillespie, M. K., Langley, K., Lee, J., Leitchenkov, G., Leuschen, C., Luyendyk, B., MacGregor, J. A., MacKie, E., Moholdt, G., Matsuoka, K., Morlighem, M., Mouginot, J., Nitsche, F. O., Nost, O. A., Paden, J., Pattyn, F., Popov, S., Rignot, E., Rippin, D. M., Rivera, A., Roberts, J. L., Ross, N., Ruppel, A., Schroeder, D. M., Siegert, M. J., Smith, A. M., Steinhage, D., Studinger, M., Sun, B., Tabacco, I., Tinto, K. J., Urbini, S., Vaughan, D. G., Wilson, D. S., Young, D. A., and Zirizzotti, A.: Bedmap3 updated ice bed, surface and thickness gridded datasets for Antarctica, Sci Data, 12, 414, https://doi.org/10.1038/s41597-025-04672-y, 2025.

Rose, K. C., Ferraccioli, F., Jamieson, S. S. R., Bell, R. E., Corr, H., Creyts, T. T., Braaten, D., Jordan, T. A., Fretwell, P. T., and Damaske, D.: Early East Antarctic Ice Sheet growth recorded in the landscape of the Gamburtsev Subglacial Mountains, Earth and Planetary Science Letters, 375, 1–12, https://doi.org/10.1016/j.epsl.2013.03.053, 2013.

Sangiorgi, F., Bijl, P. K., Passchier, S., Salzmann, U., Schouten, S., McKay, R., Cody, R. D., Pross, J., Van De Flierdt, T., Bohaty, S. M., Levy, R., Williams, T., Escutia, C., and Brinkhuis, H.: Southern Ocean warming and Wilkes Land ice sheet retreat during the mid-Miocene, Nat Commun, 9, 317, https://doi.org/10.1038/s41467-017-02609-7, 2018.

Schroeder, D. M., Blankenship, D. D., Raney, R. K., and Grima, C.: Estimating Subglacial Water Geometry Using Radar Bed Echo Specularity: Application to Thwaites Glacier, West Antarctica, IEEE Geosci. Remote Sensing Lett., 12, 443–447, https://doi.org/10.1109/LGRS.2014.2337878, 2015.

Schwanghart, W. and Scherler, D.: Short Communication: TopoToolbox 2 – MATLAB-based software for topographic analysis and modeling in Earth surface sciences, Earth Surf. Dynam., 2, 1–7, https://doi.org/10.5194/esurf-2-1-2014, 2014.

Sleep, N. H.: Mantle plumes from top to bottom, Earth-Science Reviews, 77, 231–271, https://doi.org/10.1016/j.earscirev.2006.03.007, 2006.

Smith, A. G. G., Fox, M., Schwanghart, W., and Carter, A.: Comparing methods for calculating channel steepness index, Earth-Science Reviews, 227, 103970, https://doi.org/10.1016/j.earscirev.2022.103970, 2022.

Stock, J. D. and Montgomery, D. R.: Geologic constraints on bedrock river incision using the stream power law, J. Geophys. Res., 104, 4983–4993, https://doi.org/10.1029/98JB02139, 1999.

Summerfield, M. A. and Hulton, N. J.: Natural controls of fluvial denudation rates in major world drainage basins, J. Geophys. Res., 99, 13871–13883, https://doi.org/10.1029/94JB00715, 1994.

Taylor, J., Siegert, M. J., Payne, A. J., Hambrey, M. J., O'Brien, P. E., Cooper, A. K., and Leitchenkov, G.: Topographic controls on post-Oligocene changes in ice-sheet dynamics, Prydz Bay region, East Antarctica, Geol, 32, 197, https://doi.org/10.1130/G20275.1, 2004.

https://doi.org/10.5194/egusphere-2026-847
Preprint. Discussion started: 19 February 2026

Thomson, S. N., Reiners, P. W., Hemming, S. R., and Gehrels, G. E.: The contribution of glacial erosion to shaping the hidden landscape of East Antarctica, Nature Geosci, 6, 203–207, https://doi.org/10.1038/ngeo1722, 2013.

Van Breedam, J., Huybrechts, P., and Crucifix, M.: Modelling evidence for late Eocene Antarctic glaciations, Earth and Planetary Science Letters, 586, 117532, https://doi.org/10.1016/j.epsl.2022.117532, 2022.

Van De Flierdt, T., Hemming, S. R., Goldstein, S. L., Gehrels, G. E., and Cox, S. E.: Evidence against a young volcanic origin of the Gamburtsev Subglacial Mountains, Antarctica, Geophysical Research Letters, 35, 2008GL035564, https://doi.org/10.1029/2008GL035564, 2008.

Veevers, J. J., Saeed, A., Pearson, N., Belousova, E., and Kinny, P. D.: Zircons and clay from morainal Permian siltstone at Mt Rymill (73°S, 66°E), Prince Charles Mountains, Antarctica, reflect the ancestral Gamburtsev Subglacial Mountains–Vostok Subglacial Highlands complex, Gondwana Research, 14, 343–354, https://doi.org/10.1016/j.gr.2007.12.006, 2008.

Watts, A. B.: Isostasy and Flexure of the Lithosphere, 2nd ed., Cambridge University Press, https://doi.org/10.1017/9781139027748, 2023.

Weissel, J. K. and Karner, G. D.: Flexural uplift of rift flanks due to mechanical unloading of the lithosphere during extension, J. Geophys. Res., 94, 13919–13950, https://doi.org/10.1029/JB094iB10p13919, 1989.

Wessel, P., Luis, J. F., Uieda, L., Scharroo, R., Wobbe, F., Smith, W. H. F., and Tian, D.: The Generic Mapping Tools Version 6, Geochem Geophys Geosyst, 20, 5556–5564, https://doi.org/10.1029/2019GC008515, 2019.

Westerhold, T., Marwan, N., Drury, A. J., Liebrand, D., Agnini, C., Anagnostou, E., Barnet, J. S. K., Bohaty, S. M., De Vleeschouwer, D., Florindo, F., Frederichs, T., Hodell, D. A., Holbourn, A. E., Kroon, D., Lauretano, V., Littler, K., Lourens, L. J., Lyle, M., Pälike, H., Röhl, U., Tian, J., Wilkens, R. H., Wilson, P. A., and Zachos, J. C.: An astronomically dated record of Earth's climate and its predictability over the last 66 million years, Science, 369, 1383–1387, https://doi.org/10.1126/science.aba6853, 2020.

Whipple, K. X. and Tucker, G. E.: Dynamics of the stream-power river incision model: Implications for height limits of mountain ranges, landscape response timescales, and research needs, J. Geophys. Res., 104, 17661–17674, https://doi.org/10.1029/1999JB900120, 1999.

Winter, K., Ross, N., Ferraccioli, F., Jordan, T. A., Corr, H. F. J., Forsberg, R., Matsuoka, K., Olesen, A. V., and Casal, T. G.: Topographic Steering of Enhanced Ice Flow at the Bottleneck Between East and West Antarctica, Geophysical Research Letters, 45, 4899–4907, https://doi.org/10.1029/2018GL077504, 2018.

Wobus, C., Whipple, K. X., Kirby, E., Snyder, N., Johnson, J., Spyropolou, K., Crosby, B., and Sheehan, D.: Tectonics from topography: Procedures, promise, and pitfalls, in: Tectonics, Climate, and Landscape Evolution, Geological Society of America, https://doi.org/10.1130/2006.2398(04), 2006.

Wu, G., Ferraccioli, F., Zhou, W., Yuan, Y., Gao, J., and Tian, G.: Tectonic Implications for the Gamburtsev Subglacial Mountains, East Antarctica, from Airborne Gravity and Magnetic Data, Remote Sensing, 15, 306, https://doi.org/10.3390/rs15020306, 2023.

Young, D. A., Paden, J. D., Yan, S., Kerr, M. E., Singh, S., Vega González, A., Kaundinya, S. R., Greenbaum, J. S., Chan, K., Ng, G., Buhl, D. P., Kempf, S. D., and Blankenship, D. D.: Coupled Ice Sheet Structure and Bedrock Geology in the Deep Interior of East Antarctica: Results From Dome A and the South Pole Basin, Geophysical Research Letters, 52, e2025GL115729, https://doi.org/10.1029/2025GL115729, 2025.

https://doi.org/10.5194/egusphere-2026-847
Preprint. Discussion started: 19 February 2026

Zondervan, J. R., Hilton, R. G., Dellinger, M., Clubb, F. J., Roylands, T., and Ogrič, M.: Rock organic carbon oxidation CO2
930 release offsets silicate weathering sink, Nature, 623, 329–333, https://doi.org/10.1038/s41586-023-06581-9, 2023.